

This is an Open Access document downloaded from ORCA, Cardiff University's institutional repository:<https://orca.cardiff.ac.uk/id/eprint/126285/>

This is the author's version of a work that was submitted to / accepted for publication.

Citation for final published version:

Khajah, Tahsin, Antoine, Xavier and Bordas, Stéphane P. A. 2019. B-Spline FEM for time-harmonic acoustic scattering and propagation. *Journal of Theoretical and Computational Acoustics* 27 (03) , 1850059. 10.1142/S2591728518500597

Publishers page: <http://dx.doi.org/10.1142/S2591728518500597>

Please note:

Changes made as a result of publishing processes such as copy-editing, formatting and page numbers may not be reflected in this version. For the definitive version of this publication, please refer to the published source. You are advised to consult the publisher's version if you wish to cite this paper.

This version is being made available in accordance with publisher policies. See <http://orca.cf.ac.uk/policies.html> for usage policies. Copyright and moral rights for publications made available in ORCA are retained by the copyright holders.



B-Spline FEM for Time-Harmonic Acoustic Scattering and Propagation

Tahsin Khajah

*Department of Mechanical Engineering
University of Texas at Tyler, Tyler, TX 75707, USA
tkhajah@uttyler.edu*

Xavier Antoine

*Institut Elie Cartan de Lorraine
Université de Lorraine, France
Inria Nancy-Grand Est, SPHINX Team
F-54506, Vandoeuvre-lès-Nancy Cedex, France*

Stéphane P. A. Bordas

*Legato-Team, Institute of Computational Engineering
University of Luxembourg, Luxembourg
Institute of Mechanics and Advanced Materials
Cardiff University School of Engineering, UK
Department of Medical Research, China Medical University Hospital
China Medical University, Taichung, Taiwan*

Received 24 December 2017

Accepted 18 September 2018

Published 21 January 2019

We study the application of a B-splines Finite Element Method (FEM) to time-harmonic scattering acoustic problems. The infinite space is truncated by a fictitious boundary and second-order Absorbing Boundary Conditions (ABCs) are applied. The truncation error is included in the exact solution so that the reported error is an indicator of the performance of the numerical method, in particular of the size of the pollution error. Numerical results performed with high-order basis functions (third or fourth order) showed no visible pollution error even for very high frequencies. To prove the ability of the method to increase its accuracy in the high frequency regime, we show how to implement a high-order Padé-type ABC on the fictitious outer boundary. The above-mentioned properties combined with exact geometrical representation make B-Spline FEM a very promising platform to solve high-frequency acoustic problems.

Keywords: Time harmonic acoustic; scattering; high frequency.

1. Introduction

The purpose of this paper is to investigate the performance of B-Spline-based Finite Element Method (FEM) for solving time-harmonic acoustic wave scattering and acoustic wave propagation problems, most particularly for small wavelengths. To fix the notations, let us consider Ω^- as a d -dimensional ($d = 1, 2, 3$) scattering-bounded domain of \mathbb{R}^d , with shape $\Gamma := \partial\Omega^-$. We introduce the associated exterior (i.e. unbounded) domain of propagation $\Omega^+ := \mathbb{R}^d / \overline{\Omega^-}$. Then, solving the scattering problem leads to computing the wave field u , solution to the Boundary-Value Problem (BVP): given an incident (plane wave) field u^{inc} , find u such that

$$\begin{aligned} \Delta u + k^2 u &= 0 \quad \text{in } \Omega^+, \\ \partial_{\mathbf{n}_\Gamma} u &= \mathbf{g} := -\partial_{\mathbf{n}_\Gamma} u^{\text{inc}} \quad \text{on } \Gamma, \\ \lim_{|\mathbf{x}| \rightarrow +\infty} |\mathbf{x}|^{(d-1)} \left(\nabla u \cdot \frac{\mathbf{x}}{|\mathbf{x}|} - iku \right) &= 0, \end{aligned} \tag{1}$$

where Δ is the Laplacian operator, ∇ the gradient operator and \mathbf{n}_Γ is the outward-directed unit normal vector to Ω^- . The spatial variable is $\mathbf{x} = (x, y)$ in two dimensions and $\mathbf{x} = (x, y, z)$ in three dimensions. The wavenumber k is related to the wavelength λ by the relation: $\lambda := 2\pi/k$. The boundary condition is a Neumann (sound-hard) boundary condition (but other boundary conditions could also be considered). Denoting by $\mathbf{a} \cdot \mathbf{b}$ the Hermitian inner product of two complex-valued vector fields \mathbf{a} and \mathbf{b} , then the last equation of system (1) is known as the Sommerfeld's radiation condition^{27,73} at infinity, which represents the outgoing wave to the domain. Various numerical methods have been developed to accurately solve the scattering problem, e.g. finite elements,^{17,21,37,40,45,49,51,56,58,66,72,75,76,81,83} boundary elements,^{4-6,22,25,27,31,65,73} enriched and various modified (wave-based, hybrid, asymptotic) finite elements.^{8,9,23,24,39,40,42-44,50,55,60,61} A challenging and still outstanding question for numerics and applications is related to the so-called *high-frequency* regime, where the wavelength λ is very small compared with the characteristic length of the scatterer Ω^- .^{11,81} A first "exact" method consists in writing an integral equation on the surface Γ to represent the exterior field, and then solving this by means of a boundary element method (BEM), combined with fast evaluation algorithms (e.g. Fast Multilevel Multipole Methods (MFMMs),^{31,32,65} Adaptive Cross Approximation (ACA)^{15,88}) and preconditioned (matrix-free) Krylov subspace iterative solvers (GMRES).^{5,6,78} This approach has the very interesting property to reduce the initial problem to a finite $(d - 1)$ -dimensional problem (set on Γ) and to be relatively stable thanks to the frequency regime (typically from $n_\lambda = 5$ to 10 points per wavelength are used, with $n_\lambda = \lambda/h$, and h the meshsize). Nevertheless, the method is nontrivial to adapt to complex geometries, when the boundary conditions are modified or when a high-order of accuracy is required for the solution. In particular, developing efficient algorithms when the geometry is described with high accuracy remains an open question, most particularly for large wavenumbers k since the number of degrees

of freedom is potentially very large. Recently, it was shown that an unexpected number of studies used incorrect sign when coupling parameter of the Burton Miller method arising in BEM which leads to inefficient solutions and possibly incorrect results.⁶⁷ The use of discontinuous elements in BEM collocation and effect of super convergence was studied for acoustics.⁶⁹ It was shown that zeros of the Legendre polynomials can be used to find the optimal position of nodes and quadratic elements were identified as the most efficient element type for low error analysis.

Another standard engineering-type approach consists in truncating the exterior domain Ω^+ through the introduction of a fictitious boundary/layer Σ that surrounds the scatterer Ω^- , resulting in a bounded computational domain Ω_b with inner boundary Γ and outer boundary/layer Σ . When Σ is a boundary, an *Absorbing Boundary Condition* (ABC)^{3,14,46–48,59,70,84,85} is set on the fictitious boundary which introduces a truncation error even at the continuous level. This can be reduced by considering high-order (local) ABCs. A very popular alternative is, rather, to consider a surrounding absorbing layer and modifying the nonphysical media to obtain a Perfectly Matched Layer.^{16,18,19,26}

Truncation of the exterior domain Ω^+ will introduce an error even before domain discretization, hence called the continuous truncation error. In this paper, since our goal is to understand the quality of the B-Spline-based FEM in approximating the wave field, first we will consider *simple boundary conditions* where we can separate the continuous truncation error from the discretization error to compute *an exact reference analytical solution*. To get a fully high-order scheme for exterior acoustic problems, the truncation error should also be small or at least of the order of the approximation error and then would require the use of high-order ABCs or well-tuned PMLs. To this end, we will consider also a high-order Padé-type ABC to illustrate the flexibility of the B-Splines approximation. This choice provides an example of a higher-order ABC but would in fact need a more thorough study since additional computational difficulties then arise like proving the full stability of the global scheme, the strategy for resolving the associated sparse linear system through well-adapted domain decomposition techniques.^{20,35,36,38,41}

In the high frequency regime, the numerical solution suffers from a phase shift due to numerical dispersion which is called the *pollution error*^{11,21,57,58} of the FEM. To maintain a prescribed pollution error, the mesh density n_λ should be increased faster than the wavenumber leading to high computational cost for high frequency problems. Therefore, the FEM is limited to a upper frequency bound for which the computational cost becomes prohibitive and increasing the order of the polynomial basis functions used in conventional FEM is required to reduce the pollution error, but it does not fully eliminate it. The effects of number of elements and element types in FEM on the accuracy of the numerical results were studied in Ref. 62 where authors recommended quadratic elements provided that all field gradients are monotonic inside the elements. The pollution error of the BEM in solving acoustic problems was also investigated in Ref. 68 where in addition to amplitude error due to damping, a small phase error was observed. Hence, in addition to truncation errors, the numerical solution suffers from discretization and pollution errors which are expressed in

the following inequality describing their contribution in H^1 semi-norm³⁴:

$$\frac{\|u^{\text{ex}} - u_h\|}{\|u^{\text{ex}}\|} < C_1 \left(\frac{kh}{2p}\right)^p + C_2 k \left(\frac{kh}{2p}\right)^{2p}, \quad (2)$$

where h is the element size, and p is the basis order, u^{ex} and u_h are analytical and numerical solutions, respectively. The right-hand side terms $C_1(\frac{kh}{2p})^p$, and $C_2k(\frac{kh}{2p})^{2p}$ are the contributions of the discretization and pollution errors, respectively. For linear elements ($p = 1$), the first term of the right-hand side of Eq. (2) simplifies to C_1kh . Therefore, by keeping $kh < 1$ constant, the discretization error is controlled leading to the rule of thumb to have at least 10 elements per wavelength. However, this is not sufficient to control the pollution error described by $C_2k(\frac{kh}{2p})^{2p}$ which increases with the wavenumber k . In Ref. 82, it was shown that high-order p -type elements yield higher accuracy per degrees of freedom when compared to low-order elements. A discrete dispersive relation for high-order FEM analysis was obtained in Ref. 1 where three different behaviors were identified for the numerical dispersion. Explicit quantitative estimates were derived for the behavior and rate of decay of dispersion error. In a different study, the dispersive and dissipative behaviors of a Gauss-point mass lumped FEM was studied² where it was shown that when the frequency of the wave ω satisfies $2p + 1 \approx \omega h$, the true wave is fully resolved. Also, the absolute accuracy of the spectral element scheme was found to be $1/p$ times better than that of the finite element scheme which is consistent with Eq. (2). Novel techniques were recently proposed to reduce the pollution error. One approach is to replace the basis functions, usually a polynomial, with plane wave functions.^{44,61} Since pollution error can be viewed as a phase shift, another hybrid approach is to asymptotically approximate the phase of the solution and to reformulate the problem into an equivalent problem with a slowly varying unknown.^{8–10,12,13,22,43,86} Nevertheless, until now, the only viable solution for complex problems is to consider a sufficiently high-order polynomial basis into the FEM together with high-order meshes to represent accurately the geometry Γ .^{34,82} Furthermore, the numerical integration can be modified to minimize the dispersion. Recently, dispersion-optimized quadrature tools have been developed to implement optimally-blended quadrature rules in the context of isogeometric analysis (IGA).⁷⁷ It was shown that the optimally blended schemes can improve the convergence rate by two orders when compared to the fully integrated Galerkin method. The aim of the present paper is to analyze the quality of alternative approximation methods based on B-splines-based FEM, specifically, to investigate problems involving large wavenumbers k . The B-Spline and Nonuniform Rational Basis Spline (NURBS)-based FEM has been investigated in the context of IGA which was introduced over 10 years ago to streamline the transition from Computer-Aided Design (CAD) to Analysis.^{30,52} The central idea of the approach is to use the same shape functions to approximate the field variables as those used to describe the geometry of the domain. As the geometry of computational domains is typically provided by CAD software, it is sensible to use NURBS shape functions, which are the most commonly used functions in CAD. Since 2005, IGA has been developed within the finite element, boundary element^{64,79,80} and was enriched through partition of unity.⁷⁴ B-Spline and NURBS-based FEM benefits from exact (and smooth) geometry representation

and no loss of boundary details. This is fundamental in problems involving wave propagation or turbulence, as spurious wave scattering and vortices typically appear close to rough boundaries.^{30,52} Adopting B-Spline basis functions alleviates the meshing burden as if the CAD model is modified, any modifications are immediately inherited by the shape functions used for analysis. When coupled to boundary element approaches, this suppresses completely the generation and regeneration of the mesh.^{63,64}

When used within a finite element approach, volume parameterization is still required, but the shape optimization process is simplified.⁸⁷ A recent review of IGA and its computer implementation aspects are available in Ref. 74. GeoPDEs is an open source IGA research tool³³ which provides a flexible coding structure to perform FEM analysis with B-Spline and NURBS basis functions. The application of IGA and its performance in solving one-dimensional (1D) and two-dimensional (2D) eigenvalue and interior Helmholtz problems have been studied^{28,29,53,54} in which IGA showed superiority to conventional FEM. In particular, in Ref. 53, the performance of NURBS-based FEM in solving structural vibration and wave propagation was found superior and more robust when compared with standard C^0 continuous FEM. It was also shown that NURBS basis provides higher accuracy per degree of freedom.

However, the performance of B-Spline-based FEM in solving exterior scattering problems and related pollution and truncation errors are still not thoroughly investigated.

In this paper, we first study the performance of B-Spline FEM for solving time-harmonic exterior scattering problems in one, two and three dimensions. We consider a simple but meaningful 1D scattering problem in Sec. 2 to show the effect of pollution error. Then, In Sec. 3, we analyze 2D problems and study the performance of B-Spline FEM in estimating the scattered field from a duct and a circular cylinder where the domain truncation error is eliminated. We also make some remarks on the linear systems structures. In Sec. 4, we examine the performance of higher-order ABCs, called Padé-type ABC, well adapted to the high-frequency analysis and compare it with the second-order ABC. Scattering of a 2D submarine shape obstacle is presented in Sec. 5 where the Padé-type ABC is used to successfully truncate the computational domain close to the scatterer. We next shortly study the scattering of a sphere in Sec. 6. The in-house B-Spline-based FEM codes developed in this study were written in Matlab ® benefiting from the GeoPDEs platform for 2D and three-dimensional (3D) examples and are available for download at <https://doi.org/10.6084/m9.figshare.5379607>. Finally, Sec. 7 concludes the paper. Furthermore, a pseudo-code for the one-dimensional (1D) problem is provided in Appendix A.

2. A 1D Scattering “Toy Problem”

Now, let us come back to our physical problem by considering the simple 1D Neumann scattering problem solved in Ref. 8:

$$\partial_x^2 u + k^2 u = 0 \quad \text{in } \Omega_b = (0, 1),$$

$$\begin{aligned} \partial_x u &= ik \quad \text{at } \Gamma = \{0\}, \\ \partial_x u - ik u &= 0 \quad \text{at } \Sigma = \{1\}. \end{aligned} \tag{3}$$

The variational formulation is given as

$$\int_{\Omega_b} \{\partial_x u \partial_x \bar{v} - k^2 u \bar{v}\} dx - ik(u\bar{v})(1) = -(g\bar{v})(0), \quad \forall v \in H^1(\Omega_b). \tag{4}$$

The solution of the 1D BVP (3) is $u^{\text{ex}}(x) = e^{ikx}$, which represents the scattering of an incident plane wave by the left half space. An exact transparent boundary condition is considered for the fictitious boundary at $\Sigma = \{1\}$ using the Dirichlet-to-Neumann operator $\Lambda = ik$ on Σ , resulting in the transparent boundary condition $\partial_x u = \Lambda u$. It is shown that the Finite Element-approximated solution of the BVP described in system (3) suffers from pollution error.^{8,56,58,81} The pollution error has a direct relation with the wavenumber k and increases with frequency. It is the polynomial basis used in conventional FEM which is inadequate to represent the wavefield. Hence, it is interesting to study the performance of B-Spline FEM, in particular for high frequencies and its pollution error.

We define the density of discretization as the number of nodes (control points) per wavelength and denote it with n_λ . A Matlab code was prepared to solve the above example in B-Spline FEM context. The corresponding pseudo-code is presented in Appendix A. We plot the approximate solution u_h for $k = 40$ as well as the exact solution in Fig. 1. The density of discretization in points per wavelength is $n_\lambda = 10$. As expected, B-Spline FEM ($p = 1$) also suffers from pollution error, indeed, B-Spline functions generated with $p = 0$ and $p = 1$ orders will result in the same piecewise constant and linear functions as standard FEM shape functions. The differences are found for cases using higher order shape functions. The p th order B-Spline function has $p - 1$ continuous derivatives across the element boundaries. Each B-Spline basis is pointwise nonnegative over the entire domain

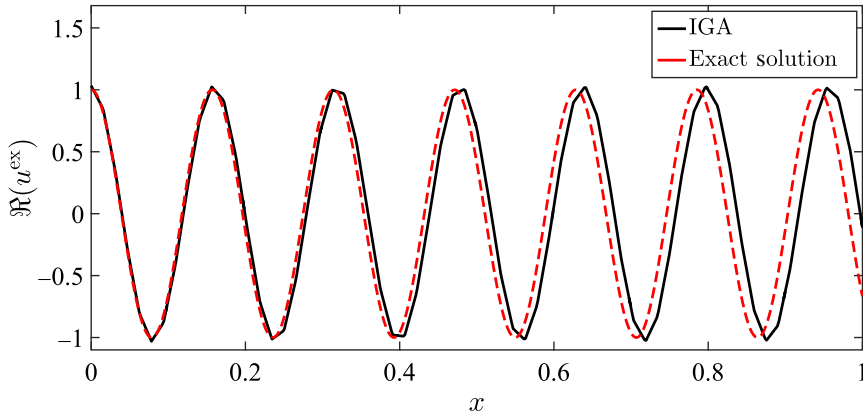


Fig. 1. The pollution error is the numerical solutions $\Re(u_h)$ of B-Spline FEM ($p = 1$) and is visible when compared with the exact solution $\Re(u^{\text{ex}})$ for $k = 40$ and $n_\lambda = 10$.

as a result, all of the entries of the mass matrix will be positive. The support of a B-Spline function of order p is always $p+1$ knot spans. Therefore, the support of higher order B-Spline functions are much larger compared to Lagrange-based FEM. The total number of functions that any given function shares support with (including itself) is $2p+1$ regardless of whether a Lagrange basis or a B-Spline basis is used. Hence, using higher order B-Spline basis functions will provide improved support compared to conventional FEM without increasing the number of required shape functions. Increasing the order of Lagrangian polynomials will increase the amplitude of oscillations in conventional FEM; this problem is eliminated in B-Spline FEM as a result of nonnegativity and noninterpolatory nature of B-Splines shape functions.

Next, we investigate the effect of increasing the basis function order on the accuracy of the numerical approximation again for discretization density $n_\lambda = 10$. As expected, increasing the order p reduces the error drastically as shown in Fig. 2. There is no visible pollution error in the B-Spline FEM approximation if we keep all the parameters unchanged and increase the order of the basis function. One can reduce the error further by increasing the discretization density n_λ . For the numerical solution $f^{\text{calc}}(\mathbf{x})$, $\mathbf{x} \in \Omega_b$, we define the relative L_2 -error (in dimension d) as

$$\epsilon_2 = \frac{\left\{ \int_{\Omega_b} |f^{\text{calc}}(\mathbf{x}) - f^{\text{ex}}(\mathbf{x})|^2 d\mathbf{x} \right\}^{1/2}}{\left\{ \int_{\Omega_b} |f^{\text{ex}}(\mathbf{x})|^2 d\mathbf{x} \right\}^{1/2}}, \tag{5}$$

where f^{ex} is the exact solution. The evolution of ϵ_2 versus the discretization density n_λ is reported in Fig. 3 for the wavenumber $k = 40$. For completeness, we also plot the curves relative to the function x^{-p} for $x = n_\lambda$. We can see that the error curves fit very well the polynomial curves. Hence, pollution error is extremely weak, most particularly when p is large enough ($p \geq 3$) even for a small density n_λ .

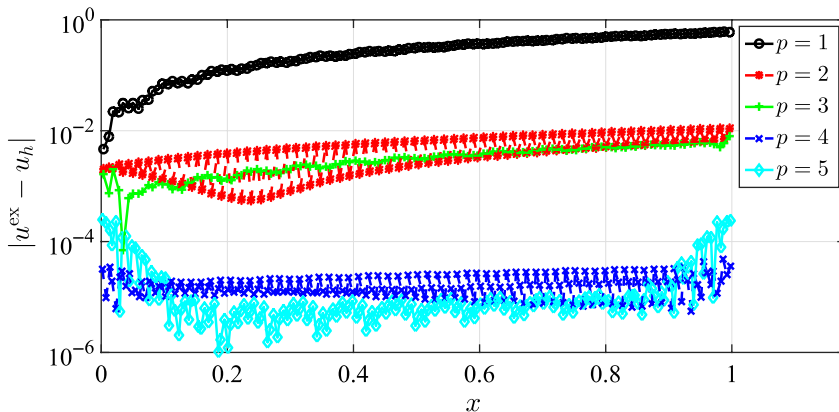


Fig. 2. Absolute error $|u^{\text{ex}} - u_h|$ for $k = 40$, $n_\lambda = 10$ and various approximation orders $p = 1, \dots, 5$.

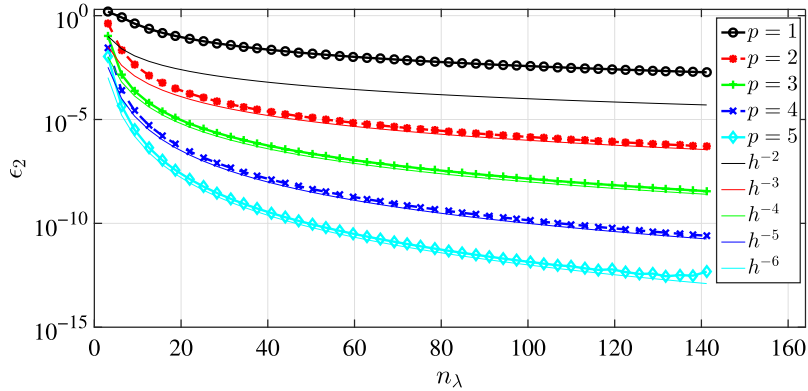


Fig. 3. Evolution of the error ϵ_2 versus the discretization density n_λ for $k = 40$ and $p = 1, \dots, 5$ (the slopes of the functions h^{p+1} are plotted for comparison).

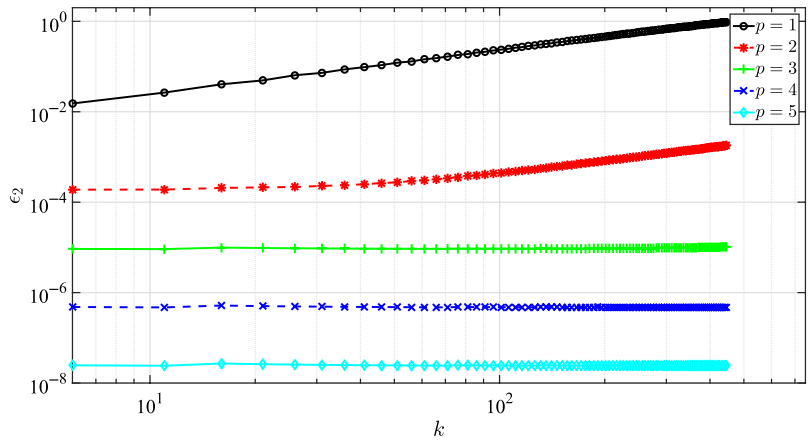


Fig. 4. Evolution of the error ϵ_2 versus the wavenumber k for $n_\lambda = 20$ and various approximation orders $p = 1, \dots, 5$. The pollution error is observable when the basis order is $p = 1$ or $p = 2$, and not visible for $p \geq 3$.

Next, we present the evolution of the L_2 -error with the wavenumber k in Fig. 4 for a fixed density $n_\lambda = 20$, where for $p = 3$ and higher, the pollution error is not visible and the error remains constant even for extremely high frequencies.

3. 2D Examples

In this section, we evaluate the performance of B-Spline FEM in solving 2D acoustic problems. First, we consider a 2D duct problem with rigid walls.⁵⁵ Next, we propose two examples of cylindrical disk scattering problems where we obtain, first the scattered field of a particular mode, and then the scattering of the disk subject to an incident plane wave. By separating the truncation error from the numerical basis approximation, we investigate the performance of B-Spline FEM in solving the 2D sound-hard scattering problem and numerically analyze the related pollution error.

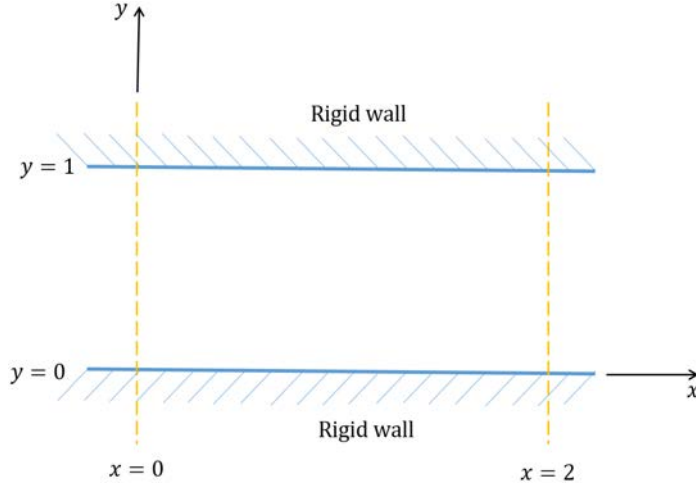


Fig. 5. The duct domain.

3.1. The duct problem

The duct model is shown in Fig. 5 where $\Omega_b = [0, 2] \times [0, 1]$. We denote the outward boundary unit normal with v and assume that the lower and upper walls are rigid. We solve the Helmholtz problem stated in Eq. (6) for the acoustic pressure u :

$$\begin{aligned}
 \Delta u + k^2 u &= 0 && \text{in } \Omega_b, \\
 \frac{\partial u}{\partial v} &= \cos(m\pi y) && \text{on } x = 0, \\
 \frac{\partial u}{\partial v} + iku &= 0 && \text{on } x = 2, \\
 \frac{\partial u}{\partial v} &= 0 && \text{on } y = 0, 1,
 \end{aligned} \tag{6}$$

where $m \in \mathbb{N}$ is the mode number. An inhomogeneous boundary condition is applied on the inlet boundary ($x = 0$) and an absorbing (and transparent for $m = 0$) boundary condition is set on the outlet boundary ($x = 2$). Since the boundaries at $y = 0, 1$ are assumed to be perfectly rigid, the normal derivative of the acoustic pressure vanishes on these boundaries. The exact solution of problem (6) with ABC is as follows:

$$u^{\text{ex}}(x, y) = \cos(m\pi y)(A_1 e^{-ik_x x} + A_2 e^{ik_x x}), \tag{7}$$

where $k_x = \sqrt{k^2 - (m\pi)^2}$ and the coefficients A_1 and A_2 are obtained from

$$i \begin{pmatrix} k_x & -k_x \\ (k - k_x)e^{-2ik_x} & (k + k_x)e^{2ik_x} \end{pmatrix} \begin{pmatrix} A_1 \\ A_2 \end{pmatrix} = \begin{pmatrix} 1 \\ 0 \end{pmatrix}.$$

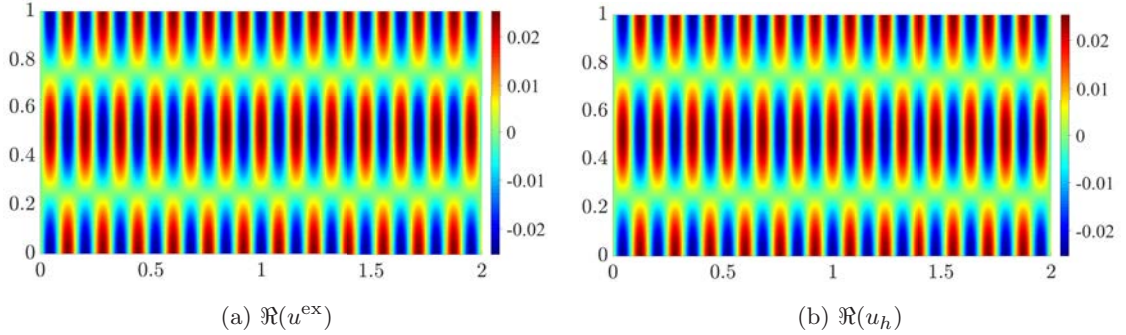


Fig. 6. Comparing (a) the real parts of the exact solution u^{ex} and (b) the numerical solution u_h for $k = 40$, $m = 2$, $p = 3$ and $n_\lambda = 10$.

Solving this 2×2 linear system, we are able to get the expression of the solution to the duct problem with ABC. This is a very interesting point since we therefore can only focus the analysis on the finite-dimensional approximation without including the (continuous) truncation error. The cut-off frequency is $m_{\text{cut-off}} = k/\pi$. If the mode is such that $m \leq m_{\text{cut-off}}$, the solution is representing propagating modes and if $m > m_{\text{cut-off}}$, the solution corresponds to evanescent modes. The real parts of the exact and estimated B-Spline FEM solutions are presented in Figs. 6(a) and 6(b), respectively, for $k = 40$, $m = 2$ (propagative mode), $p = 3$ and $n_\lambda = 10$. The corresponding absolute error $|u^{\text{ex}} - u_h|$ is plotted in Fig. 7, the maximal value being of the order of 10^{-6} .

For the propagative mode $m = 2$, the evolution of the relative L_2 -error with respect to the discretization density n_λ is shown in Fig. 8 for $k = 40$, and according to the wavenumber k in Fig. 9, where $n_\lambda = 10$. We can see that the error is very low, decreasing strongly with p . In addition, the error does not seem to depend on k as observed in Fig. 9, meaning that the pollution error is negligible.

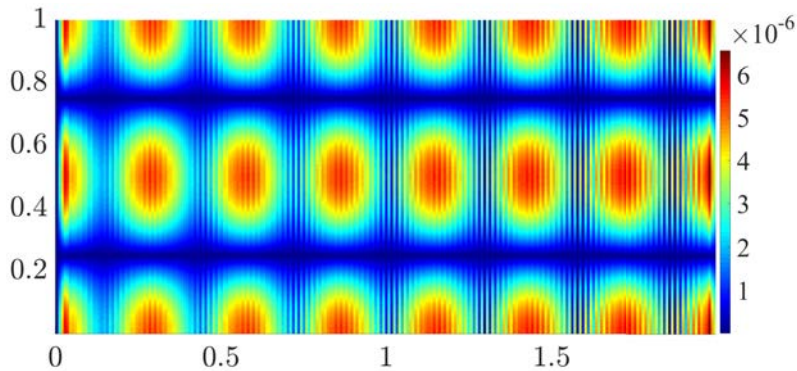


Fig. 7. Absolute error $|u^{\text{ex}} - u_h|$ for $k = 40$, $m = 2$, $p = 3$ and $n_\lambda = 10$.

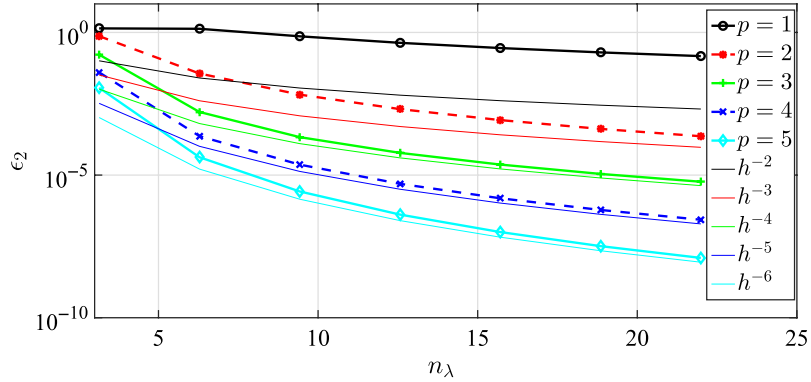


Fig. 8. Evolution of the error ϵ_2 versus the discretization density n_λ , for $k = 40$, $m = 2$ and $p = 1, \dots, 5$.

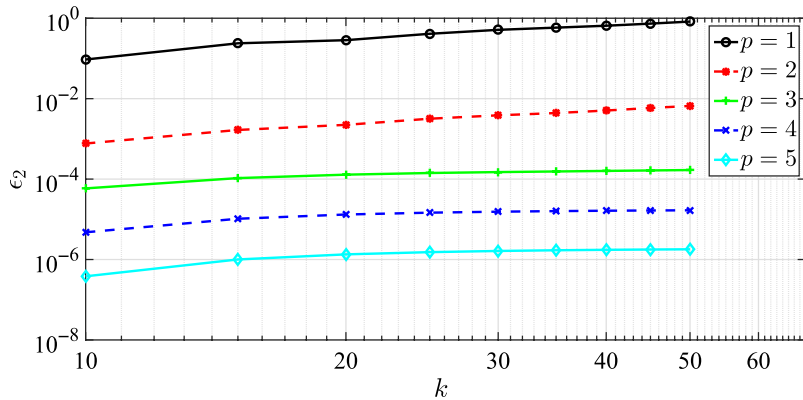


Fig. 9. Evolution of the error ϵ_2 versus the wavenumber k for $m = 2$, $n_\lambda = 10$ and $p = 1, \dots, 5$.

3.2. The sound-hard circular cylinder problem

To further study the performance of B-Spline FEM, we analyze the scattering by a 2D circular cylinder $\Omega^- = \mathcal{D}_0$ of radius R_0 centered at the origin, with boundary $\Gamma = \mathcal{C}_0$ (circle of radius R_0). The scatterer is surrounded by an outer fictitious circular boundary $\Sigma = \mathcal{C}_1$, again centered at the origin and with radius $R_1 > R_0$. Hence, the computational domain Ω_b is the annulus bounded between the inner \mathcal{C}_0 and outer \mathcal{C}_1 boundaries. On the outer boundary, we set the symmetrical second-order Bayliss–Turkel ABC³ given by

$$\partial_{\mathbf{n}_\Sigma} u - \mathcal{B}u = 0 \quad \text{on } \Sigma, \quad (8)$$

with $\mathcal{B}u := \partial_s(\alpha \partial_s u) - \beta u$ and

$$\alpha := -\frac{1}{2ik \left(1 + \frac{i\kappa}{k}\right)}, \quad \beta = -ik + \frac{\kappa}{2} - \frac{\kappa^2}{8(\kappa - ik)}. \quad (9)$$

We set \mathbf{n}_Σ as the outwardly directed unit normal to Σ and $\partial_{\mathbf{n}_\Sigma} := \partial_r$ as the normal derivative. In addition, $\kappa = R_1^{-1}$ is the curvature of $\Sigma := C_1$ and $\partial_s := R_1^{-1}\partial_\phi$ is the first-order curvilinear derivative on C_1 . In the above expressions, the polar coordinate system is denoted by (r, ϕ) .

3.2.1. Scattering by a sound-hard circular cylinder: Mode-by-mode analysis

We consider an incident wave with a fixed mode m which is described as

$$u_m^{\text{inc}}(\mathbf{x}) = J_m(kr)e^{im\phi} \quad m \in \mathbb{Z}, \quad (10)$$

where J_m is the m th order Bessel's function. The exact exterior modal solution u_m^{ex} to the truncated scattering problem of the inner sound-hard circular cylinder \mathcal{C}_0 in polar coordinate (r, ϕ) is given as

$$u_m^{\text{ex}}(\mathbf{x}) = (a_m H_m^{(1)}(kr) + b_m H_m^{(2)}(kr))e^{im\phi}, \quad R_1 \geq r \geq R_0, \quad m \in \mathbb{Z}. \quad (11)$$

The functions $H_m^{(1)}$ and $H_m^{(2)}$ are the first- and second-kind Henkel functions of order m , respectively. The Neumann boundary condition is applied on \mathcal{C}_0 and the ABC on \mathcal{C}_1 , resulting in the following linear system of equations to obtain the two unknown coefficients a_m and b_m :

$$a_m = -\frac{A_{22}^m J_m'(kR_0)}{D_m}, \quad b_m = \frac{A_{21}^m J_m'(kR_0)}{D_m}, \quad (12)$$

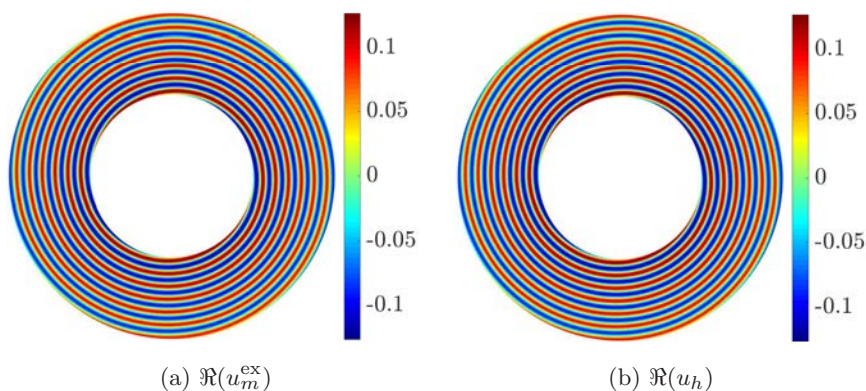
where $D_m = A_{11}^m A_{22}^m - A_{21}^m A_{12}^m$ and

$$\begin{cases} A_{11}^m = H_m^{(1)}(kR_0), & A_{21}^m = kH_m^{(1)}(kR_1) - \mathcal{B}_m H_m^{(1)}(kR_1), \\ A_{12}^m = H_m^{(2)}(kR_0), & A_{22}^m = kH_m^{(2)}(kR_1) - \mathcal{B}_m H_m^{(2)}(kR_1), \\ \mathcal{B}_m = -\left(\alpha_m \frac{m^2}{R_1^2} + \beta_m\right), & \alpha_m = -\frac{1}{2ik} \left(1 + \frac{i}{kR_1}\right)^{-1}, \\ \beta_m = -ik + \frac{1}{2R_1} + \frac{1}{8iR_1(i + kR_1)}. \end{cases}$$

The notation $f' := \partial_r f$ designates the radial derivative of a given function $f(r)$. Quite similarly to the duct problem, the modes $m \in \mathbb{N}$ such that $|m| < kR_0$ are propagating. For $|m| > kR_0$, the modes are evanescent (and therefore are not visible in the far-field since they do not propagate). A special case corresponds to $|m| \approx kR_0$, which is related to grazing modes that are tangent to the scatterer (generating glancing rays). The modal analysis is meaningful since we can understand the accuracy of B-Spline approximations for the spatial frequencies m and the dimensionless wavenumber kR_0 . In addition, this also helps in clarifying what can be expected for the case of the scattering of a plane wave by the disk since the exact solution is built as a modal series expansion of the elementary mode solutions.



Fig. 10. Outline of the patches.


 Fig. 11. Comparing (a) the real parts of the exact solution u_m^{ex} and (b) the numerical B-Spline FEM solution u_h for $k = 40$, $m = 2$, $p = 3$ and $n_\lambda = 10$.

We fix $R_0 = 1$ and $R_1 = 2$. The domain model was generated using four identical patches as shown in Fig. 10. We report the real parts of u_m^{ex} and u_h in Fig. 11 where the wavenumber is $k = 40$ and $m = 2$ (which is a propagating mode since $m = 2 \leq kR_0 = 40$). The order of the method is $p = 3$ for a density of discretization points per wavelength $n_\lambda = 10$. We clearly see that the wavefield is accurately computed since the absolute error $|u_m^{\text{ex}} - u_h|$ is below 10^{-5} as it can be deduced from Fig. 12. The convergence graph presented in Fig. 13 shows the effect of increasing the discretization density n_λ for various orders p of the underlying Spline basis function on the relative L_2 -error ϵ_2 for $k = 40$ and $m = 2$. We see that the error curves follow the slopes of the curves h^{p+1} . The evolution of the relative error ϵ_2 with respect to the wavenumber k is plotted in Fig. 14, for $m = 2$, with various approximation orders p of B-Spline FEM and $n_\lambda = 10$. We can observe that the accuracy does not strongly depend on k for a fixed density when $p \geq 3$.

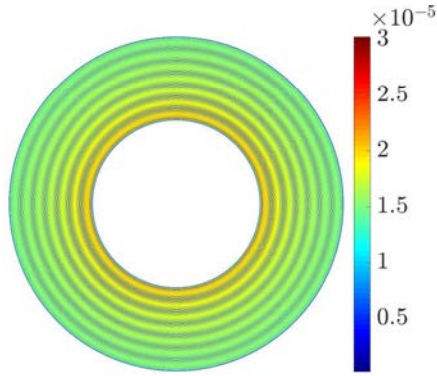


Fig. 12. Absolute error $|u_m^{\text{ex}} - u_h|$ for $k = 40$, $m = 2$, $p = 3$ and $n_\lambda = 10$.

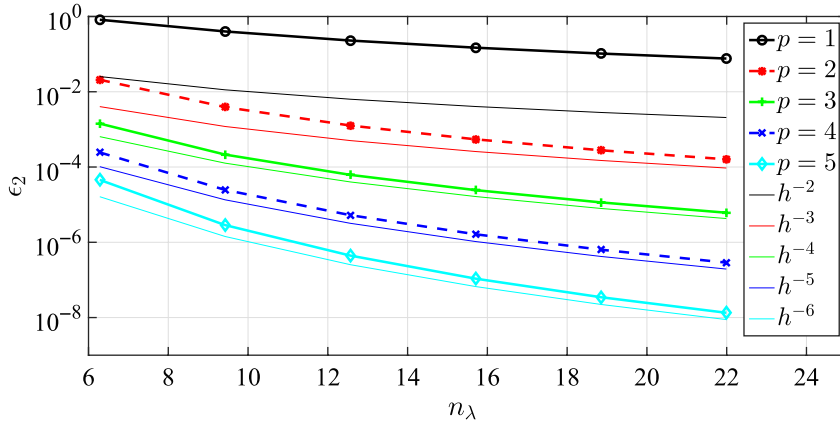


Fig. 13. Evolution of the error ϵ_2 versus the discretization density n_λ for $k = 40$, $m = 2$ and $p = 1, \dots, 5$.

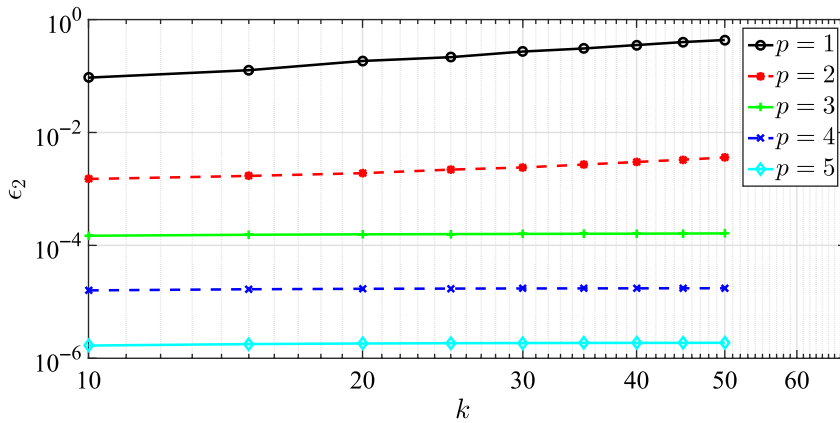


Fig. 14. Evolution of the error ϵ_2 versus the wavenumber k for $m = 2$, $n_\lambda = 10$ and $p = 1, \dots, 5$. The accuracy of the solution is independent of the wavenumber k for $p \geq 3$ and a fixed discretization density n_λ .

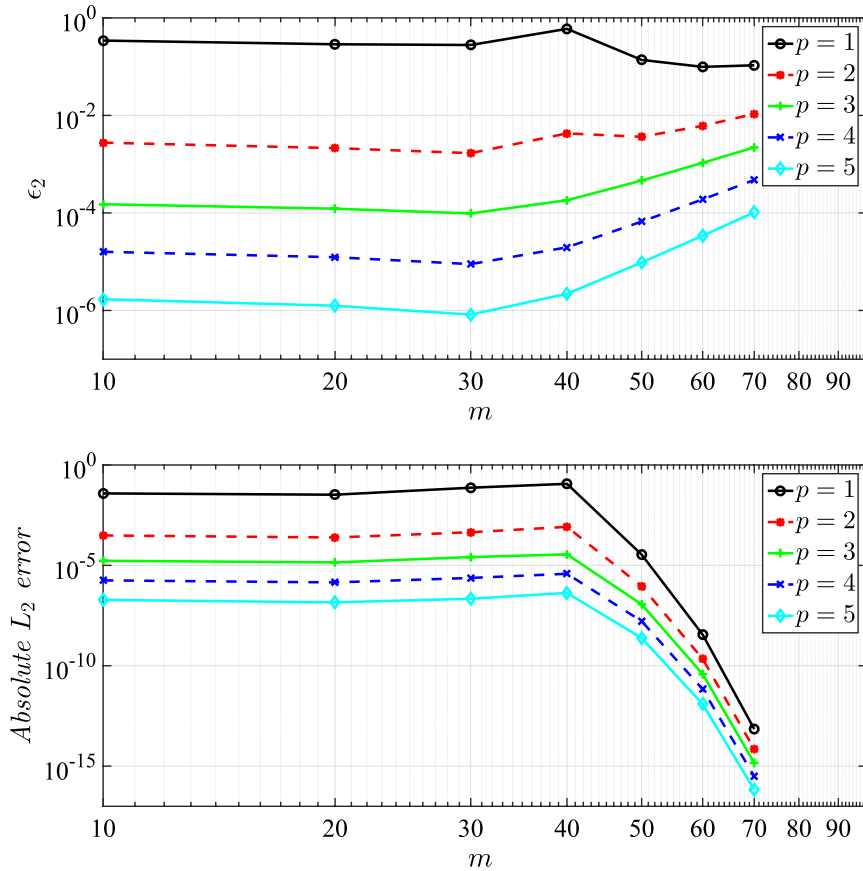


Fig. 15. Evolution of the relative error ϵ_2 (top) and absolute error (bottom) versus the mode number m for $k = 40$, $n_\lambda = 10$ and $p = 1, \dots, 5$.

One remaining question is to investigate how this error depends on m for a fixed k . To analyze this point, we report in Fig. 15(top) the evolution of the relative error ϵ_2 with respect to m and various values of p , for a fixed framework $k = 40$ and $n_\lambda = 10$. The error clearly decays strongly p -refinement. This is particularly true for the propagative modes corresponding to $m \leq kR_0 = 40$. At first sight, the situation seems to deteriorate when m is larger than $kR_0 = 40$, i.e. for the evanescent modes. This is in fact a problem related to the property that the corresponding reference solution starts quickly being very small because of the exponential decay of the evanescent modes. As a consequence, the relative error is not a suitable representation. We complete these explanations with Fig. 15(bottom) reporting the absolute error. We can indeed see that the absolute error is extremely small for the evanescent modes. From these remarks, and since the solution of the scattering of a plane wave by a circular cylinder is computed as the superposition of these modes, we can expect that similar graphs to Fig. 14 could be obtained for the full plane wave problem (see Sec. 3.2.2), most particularly because the propagating modes are the most significant modes contributing to the solution.

3.2.2. Scattering by a sound-hard circular cylinder: Plane wave scattering

In the previous section, the scattering problem of a sound-hard circular cylinder was found for given harmonics m . The solution for the full plane wave incidence can be constructed by superposition as a Fourier series expansion of these harmonics. In this section, we consider an incident plane wave $u^{\text{inc}}(\mathbf{x}) = e^{ik\mathbf{d}\cdot\mathbf{x}}$, where \mathbf{d} is the incidence direction $\mathbf{d} = (\cos(\theta^{\text{inc}}), \sin(\theta^{\text{inc}}))^T$ and θ^{inc} is the scattering angle.

Because of the symmetry of the problem, we fix the incidence direction to $\mathbf{d} = (1, 0)^T$ and the scatterer as the unit circular cylinder with $R_0 = 1$. Similar to the previous example, the second-order Bayliss–Turkel ABC (8) is placed on the circle with radius $R_1 = 2$. We consider the following exact solution⁶⁰ to analyze the pollution and approximation errors and to avoid the domain truncation error where u_m^{ex} is given by Eq. (11). To get an accurate reference solution,

$$u^{\text{ex}} = \sum_{m \in \mathbb{Z}} i^m u_m^{\text{ex}}, \quad (13)$$

we truncate the above series expansion by summing up on m from $-m^{\text{max}}$ to $m^{\text{max}} := [kR_0] + 30$ (where $[r]$ denotes the integer part of a real-valued positive number r). We report in Fig. 16 the real parts of u^{ex} (see Fig. 16(a)) and u_h (see Fig. 16(b)), where the wavenumber is $k = 40$. For B-Spline FEM, the order of the method is $p = 3$ for a density of discretization points per wavelength $n_\lambda = 10$. We clearly see that the wavefield is accurately computed since the absolute error $|u_m^{\text{ex}} - u_h|$ is below 10^{-4} as it can be deduced from Fig. 17(a). The evolution of the error with respect to the discretization density n_λ for $p = 1, \dots, 5$, is shown in Fig. 18 where the wavenumber k is equal to 40. This shows that if p is larger than 3, then the ϵ_2 -error starts being small (e.g. less than 10^{-2}) even for small densities n_λ (typically $n_\lambda \geq 6$). In addition, for $n_\lambda = 5$, we can see in Fig. 17(b) that the error remains acceptable.

The evolution of the error ϵ_2 according to the wavenumber k is depicted in Fig. 19. For this test, we fix $n_\lambda = 10$ and $p = 1, \dots, 5$ for B-Spline FEM. As we can see, the error almost

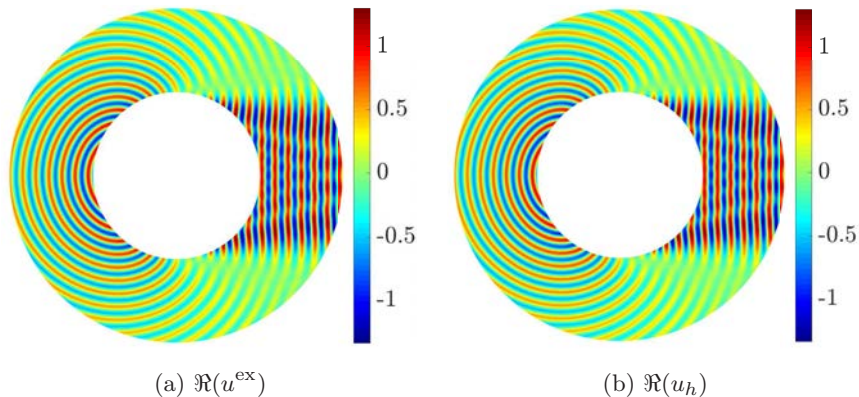


Fig. 16. Comparing the real parts of (a) the exact solution u^{ex} and (b) the numerical B-Spline FEM solution u_h for $k = 40$, $p = 3$ and $n_\lambda = 10$.

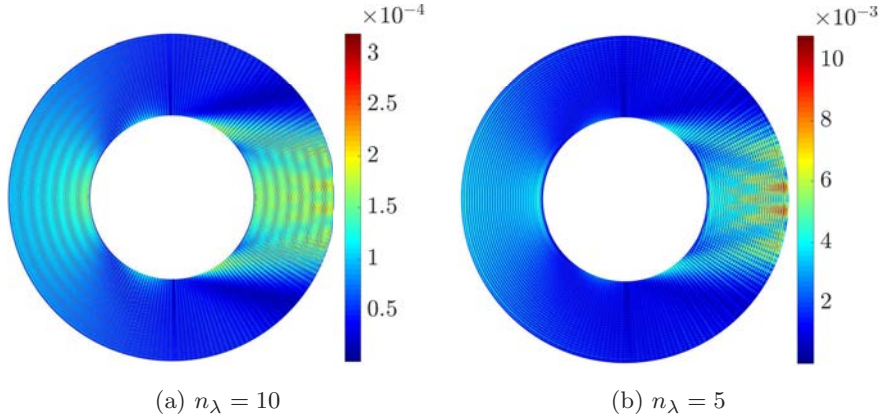


Fig. 17. Absolute error $|u^{\text{ex}} - u_h|$ for $k = 40$ and $p = 3$. The discretization density is (a) $n_\lambda = 10$ and (b) $n_\lambda = 5$.

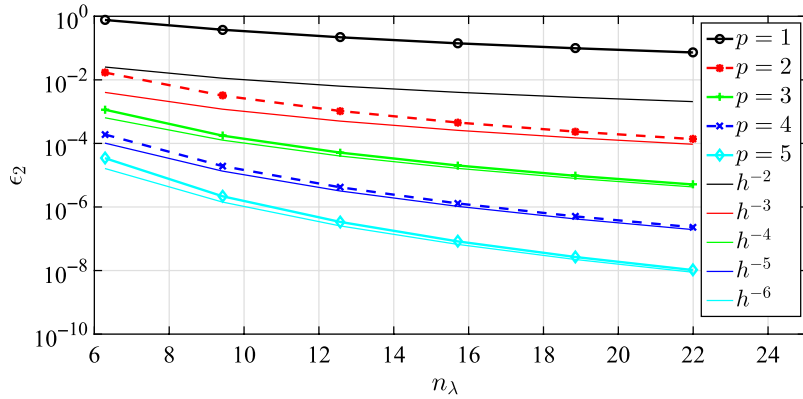


Fig. 18. Evolution of the error ϵ_2 versus the discretization density n_λ for $k = 40$ and $p = 1, \dots, 5$. The error is consistently reduced by refinement following the slopes of h^{p+1} . The error level is low for $p \geq 3$ even for the low discretization density $n_\lambda = 5$.

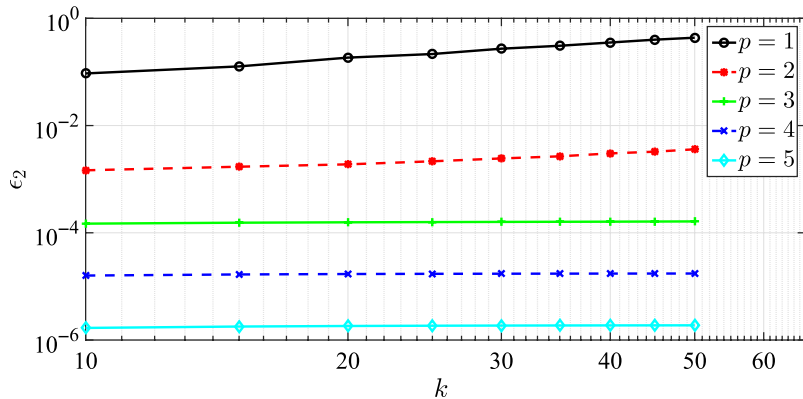


Fig. 19. Evolution of the error ϵ_2 versus the wavenumber k for $n_\lambda = 10$ and $p = 1, \dots, 5$. The numerical error does not increase with the wavenumber k when $p \geq 3$, confirming hence the small pollution error.

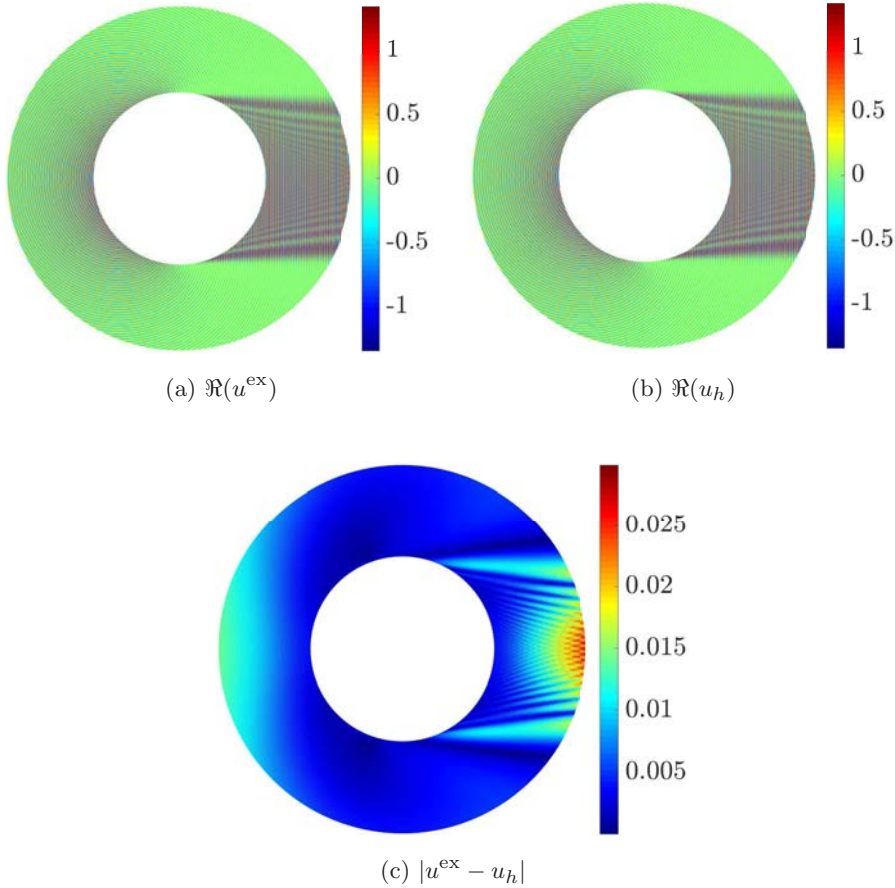


Fig. 20. Comparing the real parts of (a) the exact solution u^{ex} and (b) the numerical solution u_h and (c) absolute error $|u^{\text{ex}} - u_h|$ for $k = 200$, $p = 3$ and $n_\lambda = 5$.

does not depend on k , which means that the pollution error is very small. Again, a very good accuracy is obtained for $p \geq 3$, the error dependence on k seems to be more identifiable for the lowest-order approximations, i.e. $p = 1$ and $p = 2$. We consider now a much higher wavenumber, i.e. $k = 200$. We report in Fig. 20(b) the real part of the numerical solution for $p = 3$ and the low density of discretization points per wavelength $n_\lambda = 5$. The solution can be compared with the exact solution available in Fig. 20(a). We immediately see that the two solutions are the same. This is confirmed in Fig. 20(c) where we report the absolute error $|u^{\text{ex}} - u_h|$ between the two solutions. This error is of the order 10^{-2} which is relatively low for the discretization density of $n_\lambda = 5$.

Finally, we report now the results for a very high wavenumber $k = 500$ in Fig. 21. We provide the real parts of the exact solution u^{ex} (Fig. 21(a)) and B-Spline FEM numerical solution u_h (Fig. 21(b)). For B-Spline FEM, the order of the method is $p = 3$ for a density of discretization points per wavelength $n_\lambda = 5$. Even if there is no visible difference, plotting

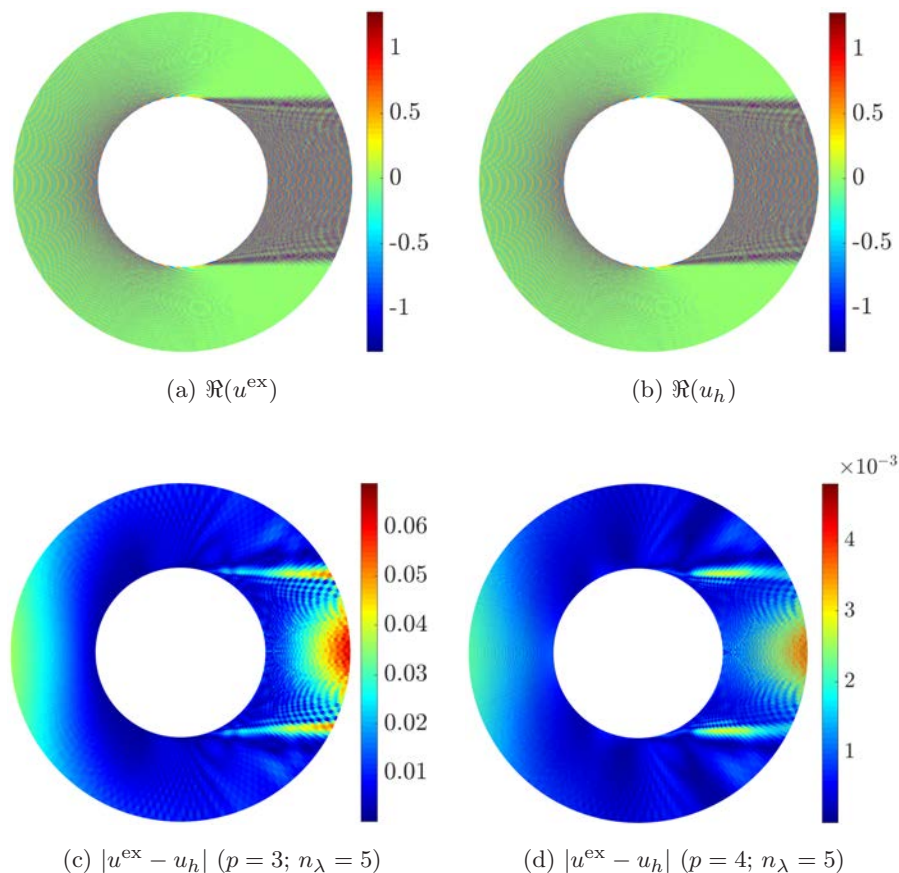


Fig. 21. Comparison of the real parts of (a) the exact solution u^{ex} and (b) the numerical B-Spline FEM solution u_h for $k = 500$, $p = 3$ and $n_\lambda = 5$. Absolute error $|u^{\text{ex}} - u_h|$ for (c) $p = 3$; $n_\lambda = 5$ and (d) $p = 4$; $n_\lambda = 5$.

the absolute error on Fig. 21(c) shows an order of about 6%. This can be made much smaller by increasing the order of approximation to $p = 4$ by keeping $n_\lambda = 5$ as seen in Fig. 21(d), leading to an error of about 10^{-3} .

3.3. Remarks on the linear system structure for B-Spline FEM

Spline bases lead to linear systems which are not as sparse as Lagrange bases. For the case of the unit circular cylinder, we report in Figs. 22(a)–22(e) the sparsity pattern of the matrices for a single patch method for various values of the order p (and for $k = 10$ and $n_\lambda = 5$). We clearly see that the bandwidth of the matrices increases with p , but in a structured way. In addition, when increasing the number of patches from one to four (see Figs. 23(a)–23(e)), we can observe a block structure of the matrix, but without increasing the number n_z of nonzero elements. Of course, increasing the order p enlarges the bandwidth of the elementary matrices related to the patches, as expected.

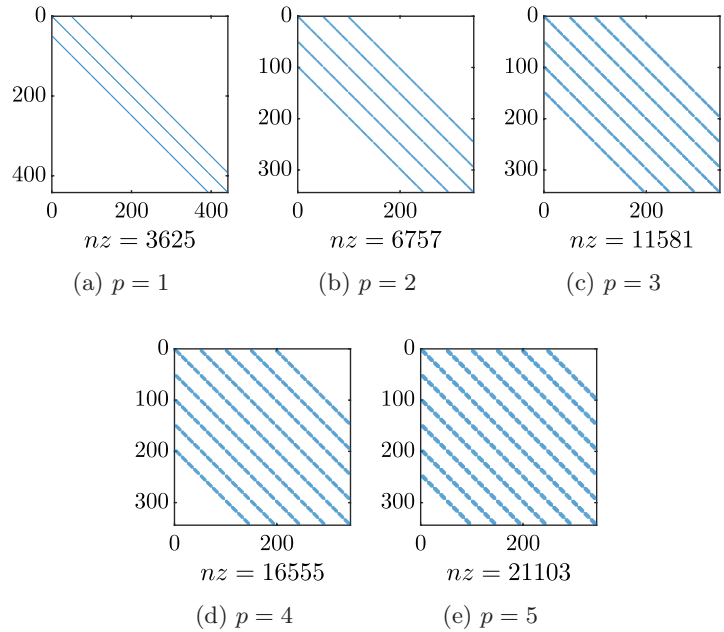


Fig. 22. Unit circular cylinder: sparsity pattern of the matrices arising in B-Spline FEM for a single patch decomposition ($k = 10$, $p = 1, \dots, 5$, $n_\lambda = 5$).

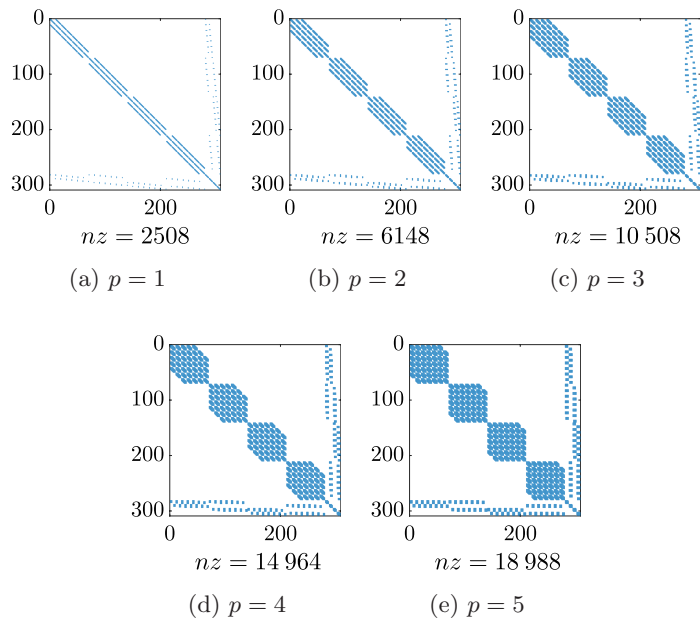


Fig. 23. Unit circular cylinder: sparsity pattern of the matrices arising in B-Spline FEM for a four patches decomposition ($k = 10$, $p = 1, \dots, 5$, $n_\lambda = 5$).

4. Increasing the Order of the ABC Based on a Padé-Type Approximate Representation

The BGT2-like ABC yields accurate numerical results in low- to mid-frequency regimes when applied on an arbitrarily shaped convex fictitious boundary Σ sufficiently far from the scatterer. The accuracy of the BGT2 ABC deteriorates as the frequency increases. In this section, we increase the order of the ABC by imposing a Padé-type ABC derived and validated in Refs. 59 and 60 for high-frequency acoustic scattering and linear FEM. We impose the radiation condition in the following form:

$$\partial_{\mathbf{n}_\Sigma} u = ik\sqrt{1 + \partial_s \left(\frac{1}{k_\epsilon^2 \partial_s} \right) u} - \frac{\kappa}{2} u + \frac{\kappa^2}{8(\kappa - ik)} u - \partial_s \left(\frac{\kappa}{2k^2} \partial_s u \right), \quad (14)$$

where s and ∂_s are the counterclockwise directed arc length and curvilinear derivative along Σ . The function κ is the curvature at a point of the artificial boundary and \sqrt{z} is the principal determination of the square root of a complex number z with branch-cut along the negative real axis which can be accurately represented by a rotating branch-cut approximation of the square root and Padé approximations.⁷¹ Furthermore, a complex wavenumber k_ϵ with small dissipation ϵ is introduced to obtain an accurate representation of the tangential rays.⁷ The modified and regularized square root operator is then approximated by

$$\sqrt{1 + \partial_s \left(\frac{1}{k_\epsilon^2} \right) \partial_s u} \approx C_0 u + \sum_{j=1}^N A_j \partial_s (k_\epsilon^{-2} \partial_s) (1 + B_j \partial_s (k_\epsilon^{-2} \partial_s))^{-1} u, \quad (15)$$

where $k_\epsilon = k + i\epsilon$ with the optimized damping parameter $\epsilon = 0.4k^{\frac{1}{3}}\kappa^{\frac{2}{3}}$.⁷ The Padé approximation of order N , denoted by R_N , and the complex coefficients C_0 , A_j and B_j are

$$\begin{aligned} \sqrt{1+z} &\approx R_N(z) = 1 + \sum_{j=1}^N \frac{a_j z}{1 + b_j z}, \\ C_0 &= e^{i\frac{\alpha}{2}} R_N(e^{-i\theta} - 1), \\ A_j &= \frac{e^{-i\theta/2} a_j}{(1 + b_j(e^{-i\theta} - 1))^2}, \\ B_j &= \frac{e^{-i\theta} b_j}{1 + b_j(e^{-i\theta} - 1)}, \end{aligned} \quad (16)$$

where α is the angle of rotation, and a_j , and b_j for $j = 1, \dots, N$, are the standard real-valued Padé coefficients given by

$$\begin{aligned} a_j &= \frac{2}{2N+1} \sin^2 \left(\frac{j\pi}{2N+1} \right), \\ b_j &= \cos^2 \left(\frac{j\pi}{2N+1} \right). \end{aligned} \quad (17)$$

Finally, the approximation of Padé-type ABC of order N is

$$\partial_{\mathbf{n}_\Sigma} u = ik \left(C_0 u + \sum_{j=1}^N A_j \phi_j \right) - \frac{\kappa}{2} u + \frac{\kappa^2}{8(\kappa - ik)} u - \partial_s \left(\frac{\kappa}{2k^2} \partial_s u \right), \quad (18)$$

where the auxiliary variables ϕ_j are defined on the fictitious boundary Σ such that

$$\left(1 + B_j \partial_s \left(\frac{1}{k_\epsilon^2} \partial_s \right) \right) \phi_j = \partial_s \left(\frac{1}{k_\epsilon^2} \partial_s \right) u. \quad (19)$$

The weak form of the sound-hard scattering problem with Padé-type ABC is obtained in terms of a system of coupled bilinear forms \mathcal{A} , \mathcal{B} , \mathcal{C} and \mathcal{D}

$$\begin{cases} \mathcal{A}(u, v) + \sum_{j=1}^N \mathcal{B}_j(\phi_j, v) = b(v), \\ \mathcal{C}(u, \psi_j) + \mathcal{D}_j(\phi_j, \psi_j) = 0, \quad j = 1, \dots, N, \end{cases} \quad (20)$$

where

$$\begin{aligned} \mathcal{A}(u, v) &= \int_{\Omega} \nabla u \nabla v d\Omega - k^2 \int_{\Omega} u v d\Omega - ik C_0 \int_{\Sigma} u v d\Sigma \\ &\quad + \frac{1}{2} \int_{\Sigma} \kappa u v d\Sigma - \frac{1}{8} \int_{\Sigma} \frac{\kappa^2}{\kappa - ik} u v d\Sigma + \frac{1}{2k^2} \int_{\Sigma} \kappa \partial_s u \partial_s v d\Sigma, \end{aligned} \quad (21)$$

$$\mathcal{B}_j(\phi_j, v) = -ik A_j \int_{\Sigma} \phi_j v d\Sigma,$$

$$\mathcal{C}(u, \psi_j) = \frac{1}{k_\epsilon^2} \int_{\Sigma} \partial_s u \partial_s \psi_j d\Sigma, \quad (22)$$

$$\mathcal{D}_j(\phi_j, \psi_j) = \int_{\Sigma} \phi_j \psi_j d\Sigma - \frac{B_j}{k_\epsilon^2} \int_{\Sigma} \partial_s \phi_j \partial_s \psi_j d\Sigma.$$

In order to understand the performance of the Padé-type ABC in the context of B-Spline-based FEM, we compute the absolute error of the scattered field of the circular cylinder with radius $R_0 = 1$, where computational domain is truncated at $R_1 = 2$. To fairly compare the performance of the Padé-type ABC with BGT2, we choose the full-space exact solution for the exterior sound-hard problem

$$u^{\text{ex}}(r, \theta) = \sum_{m=0}^{\infty} \epsilon_m (-i^m) \frac{J'_m(kR_0)}{H_n^{(1)}(kR_0)} H_m^{(1)'}(kr) \cos(m\theta). \quad (23)$$

The absolute errors for Padé and BGT2 ABCs are shown in Figs. 24(a) and 24(b) for $p = 5$, $k = 250$, $n_\lambda = 5$, where the number of Padé terms and the rotation angles are set to $N = 2$,

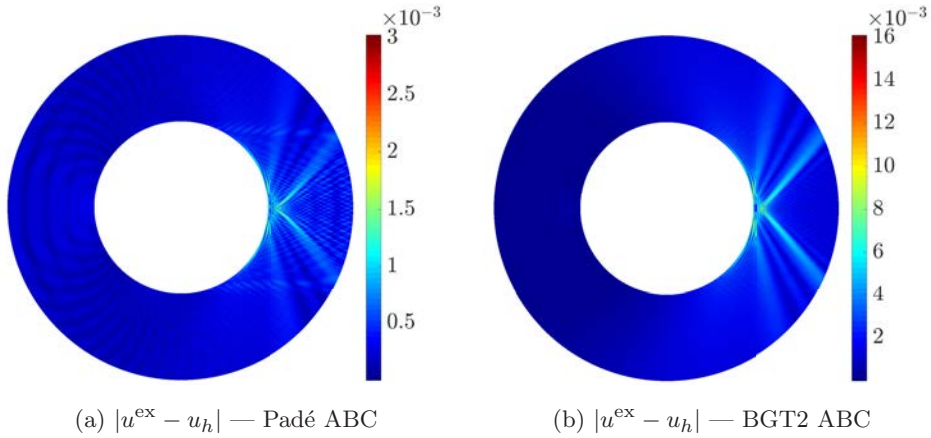


Fig. 24. Comparison of the absolute error in the computational domain for (a) Padé ABC ($N = 2$ and $\alpha = \pi/6$) and (b) BGT2 ABC for $k = 250$, $p = 5$, $n_\lambda = 5$.

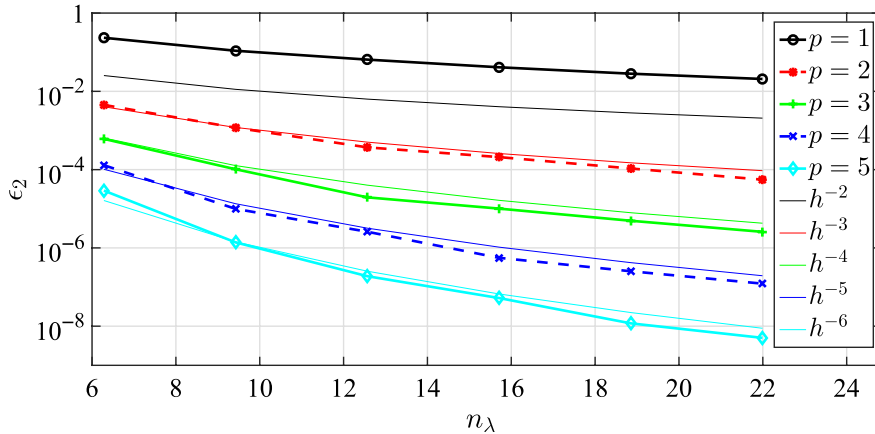


Fig. 25. Evolution of the error ϵ_2 versus the discretization density n_λ for $k = 40$ and $p = 1, \dots, 5$. Padé ABC with $\alpha = \pi/6$ and 2 terms was imposed on the artificial boundary. The error is consistently reduced by refinement following the slopes of h^{p+1} . The error was calculated with respect to a highly refined numerical solution.

and $\alpha = \pi/6$, respectively. The optimal number of Padé terms, denoted by N , may vary with the discretization density (this will be further studied in a forthcoming analysis). The evolution of relative L_2 error of the circular cylinder subjected to plane wave with respect to the discretization density, n_λ , is shown in Fig. 25 for $k = 40$, and $p = 1, \dots, 5$. The error evolution follows the slope of h^{p+1} . The error was calculated with respect to a highly refined numerical solution with Padé ABC. Next, we study the evolution of the pollution error with the wavenumber k in Fig. 26 for $n_\lambda = 10$ and $p = 1, \dots, 5$. It is noteworthy that the pollution is nonvisible for basis orders $p = 3, \dots, 5$.

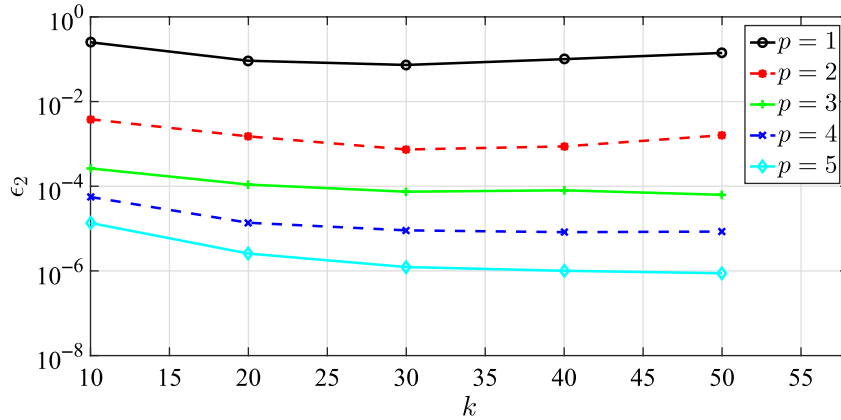


Fig. 26. Evolution of the error ϵ_2 versus the wavenumber k for $n_\lambda = 10$ and $p = 1, \dots, 5$. Padé ABC with $\alpha = \pi/6$ and 2 terms was imposed on the artificial boundary. The error was calculated with respect to an highly refined numerical solution.

5. Scattering by a Sound-Hard Submarine-Like Object

We consider a more realistic shape in this section by generating a multi-patch model of the submarine-shaped scatterer composed of 19 patches as shown in Fig. 27. The total length of the submarine is 3, the length of the hatch is 0.35 and its diameter is 0.5. We apply the Padé-type ABC at the fictitious boundary at $R_1 = 2$. We define the discretization density based on the number of degrees of freedom on the artificial boundary and maintain the same density of control points in radial direction. Padé-type ABC is imposed on the artificial boundary at $R_1 = 2$, where $N = 8$ and $\alpha = \pi/6$. Since there is no analytical solution available for this example, we use a highly refined reference solution to study the convergence of the method. The scattered and total fields are plotted in Figs. 28(a) and 28(b) for $k = 100$ and $p = 5$. The convergence of the relative L_2 error with discretization density n_λ is shown in Fig. 29 where the numerical solution is converging with h -, and p -refinement to the overly refined

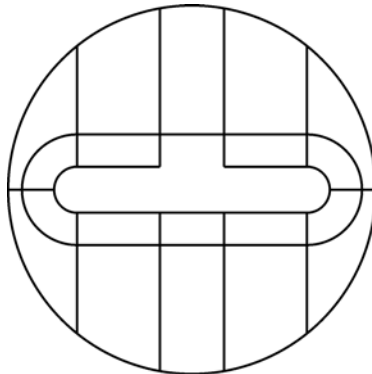


Fig. 27. The 2D submarine model made of 19 patches.

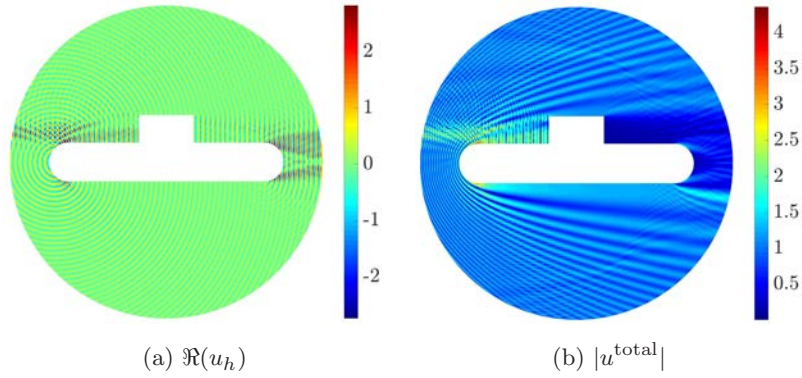


Fig. 28. Numerical solution of the submarine-shaped scatterer with Padé-type ABC with $N = 8$ and $\alpha = \pi/6$: (a) real part of the scattered field and (b) absolute value of the total field.

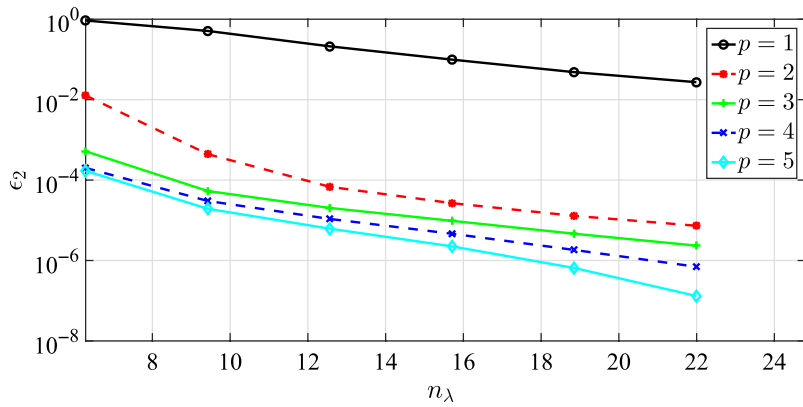


Fig. 29. Evolution of the relative L_2 error with discretization density, n_λ , for the submarine shaped scatterer with Padé ABC ($N = 8$ and $\alpha = \pi/6$) for $k = 40$ and $p = 1, \dots, 5$.

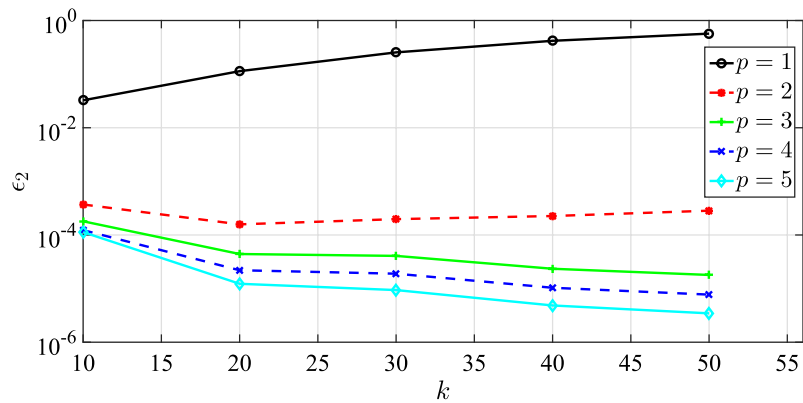


Fig. 30. Evolution of the relative L_2 error with wavenumber, k , for the submarine-shaped scatterer with Padé ABC ($N = 8$ and $\alpha = \pi/6$) for $n_\lambda = 10$ and $p = 1, \dots, 5$.

numerical solution. Similar to the previous section, we also present the evolution of L_2 error with wavenumber k in Fig. 30. It is evident that the pollution error is well under control when the basis order is equal or higher than $p = 3$.

6. Scattering of a Plane Wave by a Sound-Hard Sphere

We propose a 3D benchmark test consisting of the scattering of the plane wave $u^{\text{inc}} = e^{i\mathbf{k}\cdot\mathbf{x}}$ by a sound-hard sphere centered at the origin and with radius $R_0 = 1$. We truncate the infinite spatial domain by using the simplest ABC, i.e. the Sommerfeld radiation condition: $\partial_r u - iku = 0$, on an outer fictitious spherical boundary $\Sigma = \mathcal{S}_1$, centered at the origin, with radius $R_1 > R_0$. To separate the truncation error from the B-Spline FEM approximation error, we compute the exact solution by applying the Neumann boundary condition on $R_0 = 1$ and the ABC at $R_1 = 2$ to include the possible reflection due to the truncation. This leads to the exact solution

$$u^{\text{ex}}(\mathbf{x}) = \frac{1}{4\pi} \sum_{n=0}^{\infty} (2n+1)(A_n h_n^{(1)}(kR) + B_n h_n^{(2)}(kR)) P_n(\hat{\mathbf{x}} \cdot \hat{\mathbf{k}}), \quad (24)$$

with $\mathbf{x} := R\hat{\mathbf{x}}$ ($R = |\mathbf{x}|$), $\mathbf{k} := k\hat{\mathbf{k}}$, $h_n^{(1)}$ and $h_n^{(2)}$ the spherical Hankel's functions of the first- and second-kind, respectively, and P_n the Legendre polynomial of order n . The coefficients A_n and B_n are obtained by solving the 2×2 system of equations

$$\begin{pmatrix} h_n^{(1)'}(kR_0) & h_n^{(2)'}(kR_0) \\ h_n^{(1)'}(kR_1) - ih_n^{(1)}(kR_1) & h_n^{(2)'}(kR_1) - ih_n^{(2)}(kR_1) \end{pmatrix} \begin{pmatrix} A_n \\ B_n \end{pmatrix} = \mathbf{b}_n, \quad (25)$$

with

$$\mathbf{b}_n = \begin{pmatrix} -4\pi i^n j_n'(kR_0) \\ 0 \end{pmatrix}, \quad (26)$$

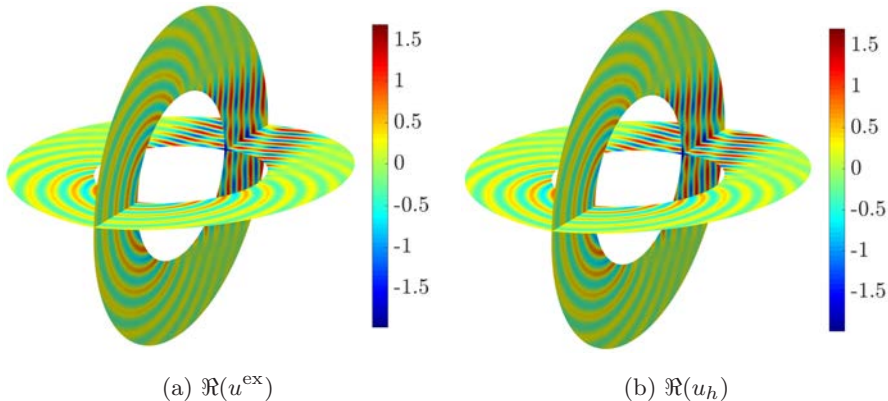


Fig. 31. Comparison of the real parts of (a) the exact solution u^{ex} and (b) the numerical solution u_h for $k = 25$, $p = 3$ and $n_\lambda = 5$.

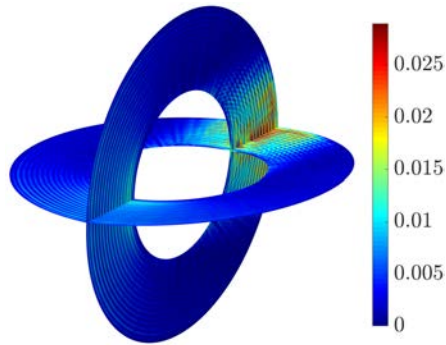


Fig. 32. The absolute error $|u^{\text{ex}} - u_h|$, $k = 25$, $p = 3$, $n_\lambda = 5$.

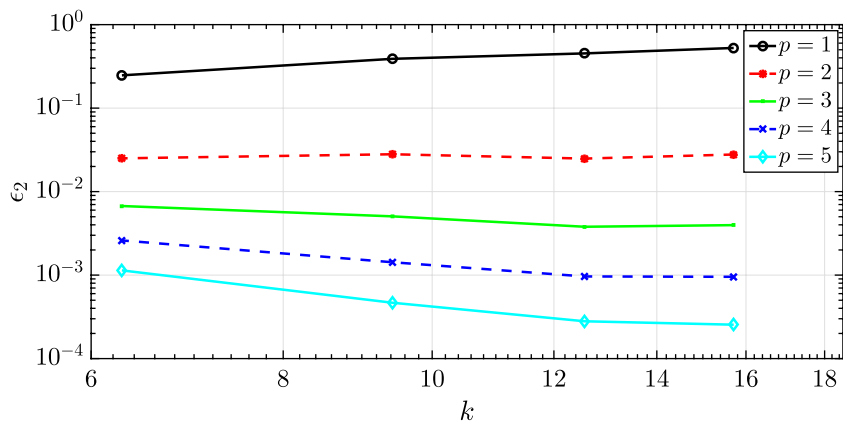


Fig. 33. Evolution of the error ϵ_2 versus the wavenumber k for $n_\lambda = 8$ and $p = 1, \dots, 5$.

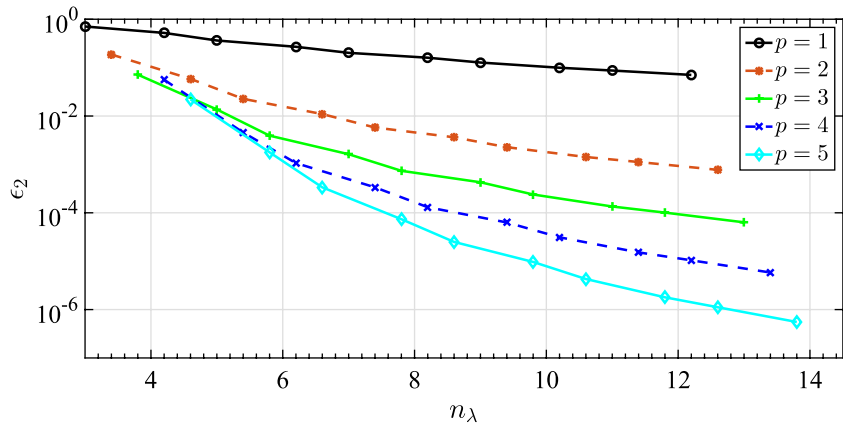


Fig. 34. Evolution of the error ϵ_2 versus the discretization density n_λ for $k = 10$ and $p = 1, \dots, 5$.

where j_n are the regular spherical Bessel functions. The real parts of the exact and numerical solutions are compared in Fig. 31, for the parameters $k = 25$, $p = 3$ and $n_\lambda = 5$. The corresponding absolute error $|u^{\text{ex}} - u_h|$ is shown in Fig. 32. We again observe a very good accuracy of the B-Spline FEM numerical solution. We report in Fig. 33 the evolution of the ϵ_2 error with respect to the wavenumber. We fix the density to $n_\lambda = 8$ and p varies from 1 to 5. We see that the error weakly depends on k , showing again that there is a low pollution error related to B-Spline FEM. From Fig. 34 where $k = 10$, we conclude that increasing the discretization density n_λ and the order of the basis consistently reduces the error.

7. Conclusion

In this paper, we formulated, implemented and exercised a B-Spline FEM for the Helmholtz problem in 1D, 2D and 3D problems. We used first a (simple) ABC on a fictitious boundary to truncate the infinite space. This truncation introduces an error in the numerical solution. To better study the performance of B-Spline FEM, the truncation error was included in the analytical solution so that the pollution error is distinguishable from the discretization error. It is shown that B-Spline FEM is a robust approach to contain the effects of the pollution error and that the boundary discretization errors are controllable. Furthermore, we studied a Padé-type ABC to perform a high-frequency analysis. We observe that the Padé-type ABC leads to a better accuracy than the BGT2 ABC with minimal additional computational cost. Accurate representation of the boundaries in B-Spline FEM regardless of the discretization density combined with low pollution error makes it a promising platform for scattering analysis. Our ongoing work focuses on a fair and complete comparison between NURBS-based approximations and high-order Lagrange-based FEMs. This requires precisely dealing with the error associated with the order of the approximation of the geometry and the inclusion of high-order ABCs and perfectly matched layers into NURBS-based approximations. We are also investigating the extension to electromagnetic scattering.

References

1. M. Ainsworth, Discrete dispersion relation for hp-version finite element approximation at high wave number, *SIAM J. Numer. Anal.* **42**(2) (2004) 553–575.
2. M. Ainsworth and H. A. Wajid, Dispersive and dissipative behavior of the spectral element method, *SIAM J. Numer. Anal.* **47**(5) (2009) 3910–3937.
3. X. Antoine, H. Barucq and A. Bendali, Bayliss–Turkel-like radiation conditions on surfaces of arbitrary shape, *J. Math. Anal. Appl.* **229**(1) (1999) 184–211.
4. X. Antoine, A. Bendali and M. Darbas, Analytic preconditioners for the boundary integral solution of the scattering of acoustic waves by open surfaces, *J. Comput. Acoust.* **13**(3) (2005) 477–498.
5. X. Antoine and M. Darbas, Alternative integral equations for the iterative solution of acoustic scattering problems, *Q. J. Mech. Appl. Math.* **58**(1) (2005) 107–128.
6. X. Antoine and M. Darbas, Generalized combined field integral equations for the iterative solution of the three-dimensional Helmholtz equation, *Math. Model. Numer. Anal.* **1**(41) (2007) 147–167.

7. X. Antoine, M. Darbas and Y. Y. Lu, An improved surface radiation condition for high-frequency acoustic scattering problems, *Comput. Methods Appl. Mech. Eng.* **195**(33–36) (2006) 4060–4074.
8. X. Antoine and C. Geuzaine, Phase reduction models for improving the accuracy of the finite element solution of time-harmonic scattering problems I: General approach and low-order models, *J. Comput. Phys.* **228**(8) (2009) 3114–3136.
9. R. Astley and W. Eversman, Finite element formulations for acoustical radiation, *J. Sound Vib.* **88**(1) (1983) 47–64.
10. R. J. Astley, Wave envelope and infinite elements for acoustical radiation, *Int. J. Numer. Methods Fluids* **3**(5) (1983) 507–526.
11. I. Babuska and S. Sauter, Is the pollution effect of the FEM avoidable for the Helmholtz equation considering high wave numbers? *SIAM J. Numer. Anal.* **34**(6) (1997) 2392–2423.
12. K. Baumeister, Analysis of sound propagation in ducts using the wave envelope concept, NASA technical note, National Aeronautics and Space Administration (1974).
13. K. Baumeister, U. S. N. Aeronautics, S. A. Scientific and T. I. Office, Finite-difference theory for sound propagation in a lined duct with uniform flow using the wave envelope concept, NASA technical paper. National Aeronautics and Space Administration, Scientific and Technical Information Office (1977).
14. A. Bayliss and E. Turkel, Radiation boundary conditions for wave-like equations, *Commun. Pure Appl. Math.* **33**(6) (1980) 707–725.
15. M. Bebendorf, Approximation of boundary element matrices, *Numer. Math.* **86**(4) (2000) 565–589.
16. J.-P. Bérenger, A perfectly matched layer for the absorption of electromagnetic waves, *J. Comput. Phys.* **114**(2) (1994) 185–200.
17. H. Bériot, A. Prinn and G. Gabard, Efficient implementation of high-order finite elements for Helmholtz problems, *Int. J. Numer. Methods Eng.* **106**(3) (2016) 213–240.
18. A. Bermudez, L. Hervella-Nieto, A. Prieto and R. Rodríguez, An optimal perfectly matched layer with unbounded absorbing function for time-harmonic acoustic scattering problems, *J. Comput. Phys.* **223**(2) (2007) 469–488.
19. A. Bermúdez, L. Hervella-Nieto, A. Prieto and R. Rodríguez, Perfectly matched layers for time-harmonic second-order elliptic problems, *Arch. Comput. Methods Eng.* **17**(1) (2010) 77–107.
20. Y. Boubendir, X. Antoine and C. Geuzaine, A quasi-optimal non-overlapping domain decomposition algorithm for the Helmholtz equation, *J. Comput. Phys.* **2**(231) (2012) 262–280.
21. P. Bouillard and F. Ihlenburg, Error estimation and adaptivity for the finite element method in acoustics: 2D and 3D applications, *Comput. Methods Appl. Mech. Eng.* **176**(1–4) (1999) 147–163.
22. O. P. Bruno, C. A. Geuzaine, J. A. Monro and F. Reitich, Prescribed error tolerances within fixed computational times for scattering problems of arbitrarily high frequency: The convex case, *Philos. Trans. R. Soc. Lond. A, Math. Phys. Eng. Sci.* **362**(1816) (2004) 629–645.
23. O. Cessenat and B. Despres, Application of an ultra weak variational formulation of elliptic PDEs to the two-dimensional Helmholtz problem, *SIAM J. Numer. Anal.* **35**(1) (1998) 255–299.
24. O. Cessenat and B. Despres, Using plane waves as base functions for solving time harmonic equations with the ultra weak variational formulation, *J. Comput. Acoust.* **11**(2) (2003) 227–238.
25. S. N. Chandler-Wilde, I. G. Graham, S. Langdon and E. A. Spence, Numerical-asymptotic boundary integral methods in high-frequency acoustic scattering, *Acta Numer.* **21** (2012) 89–305.
26. W. Chew and W. Weedon, A 3D perfectly matched medium from modified Maxwell’s equations with stretched coordinates, *Microw. Opt. Technol. Lett.* **7**(13) (1994) 599–604.

27. D. Colton and R. Kress, *Integral Equation Methods in Scattering Theory*, Pure and Applied Mathematics (Wiley, New York, 1983).
28. L. Coox, E. Deckers, D. Vandepitte and W. Desmet, A performance study of nurbs-based isogeometric analysis for interior two-dimensional time-harmonic acoustics, *Comput. Methods Appl. Mech. Eng.* **305** (2016) 441–467.
29. J. Cottrell, A. Reali, Y. Bazilevs and T. Hughes, Isogeometric analysis of structural vibrations, *Comput. Methods Appl. Mech. Eng.* **195**(41–43) (2006) 5257–5296.
30. J. A. Cottrell, T. J. R. Hughes and Y. Bazilevs, *Isogeometric Analysis: Toward Integration of CAD and FEA*, 1st edn. (Wiley, Chichester, 2009).
31. M. Darbas, E. Darrigrand and Y. Lafranche, Combining analytic preconditioner and fast multipole method for the 3D Helmholtz equation, *J. Comput. Phys.* **236** (2013) 289–316.
32. E. Darve, The fast multipole method: Numerical implementation, *J. Comput. Phys.* **160**(1) (2000) 195–240.
33. C. de Falco, A. Reali and R. Vázquez, Geopdes: A research tool for isogeometric analysis of {PDEs}, *Adv. Eng. Softw.* **42**(12) (2011) 1020–1034.
34. A. Deraemaeker, I. Babuka and P. Bouillard, Dispersion and pollution of the FEM solution for the Helmholtz equation in one, two and three dimensions, *Int. J. Numer. Methods Eng.* **46**(4) (1999) 471–499.
35. B. Després, Décomposition de domaine et problème de Helmholtz, *C. R. Acad. Sci. Paris* **1**(6) (1990) 313–316.
36. B. Després, P. Joly and J. E. Roberts, A domain decomposition method for the harmonic Maxwell equations, in *Iterative Methods in Linear Algebra* (Brussels, 1991), pp. 475–484.
37. R. Djellouli, C. Farhat, A. Macedo and R. Tezaur, Finite element solution of two-dimensional acoustic scattering problems using arbitrarily shaped convex artificial boundaries, *J. Comput. Acoust.* **8**(1) (2000) 81–99.
38. C. Farhat, P. Avery, R. Tezaur and J. Li, FETI-DPH: A dual-primal domain decomposition method for acoustic scattering, *J. Comput. Acoust.* **13**(3) (2005) 499–524.
39. C. Farhat, I. Harari and L. Franca, The discontinuous enrichment method, *Comput. Methods Appl. Mech. Eng.* **190**(48) (2001) 6455–6479.
40. G. Gabard, P. Gamallo and T. Huttunen, A comparison of wave-based discontinuous Galerkin, ultra-weak and least-square methods for wave problems, *Int. J. Numer. Methods Eng.* **85**(3) (2011) 380–402.
41. M. Gander, F. Magoules and F. Nataf, Optimized Schwarz methods without overlap for the Helmholtz equation, *SIAM J. Sci. Comput.* **24**(1) (2002) 38–60.
42. K. Gerdes, A review of infinite element methods for exterior Helmholtz problems, *J. Comput. Acoust.* **8**(1) (2000) 43–62.
43. C. Geuzaine, J. Bedrossian and X. Antoine, An amplitude formulation to reduce the pollution error in the finite element solution of time-harmonic scattering problems, *IEEE Trans. Magn.* **44**(6) (2008) 782–785.
44. E. Giladi and J. Keller, A hybrid numerical asymptotic method for scattering problems, *J. Comput. Phys.* **174**(1) (2001) 226–247.
45. G. Giorgiani, D. Modesto, S. Fernández-Mández and A. Huerta, High-order continuous and discontinuous galerkin methods for wave problems, *Int. J. Numer. Methods Fluids* **73**(10) (2013) 883–903.
46. D. Givoli, High-order local non-reflecting boundary conditions: A review, *Wave Motion* **39**(4) (2004) 319–326.
47. M. Guddati and J. Tassoulas, Continued-fraction absorbing boundary conditions for the wave equation, *J. Comput. Acoust.* **8**(1) (2000) 139–156.

48. T. Hagstrom, New results on absorbing layers and radiation boundary conditions, in *Topics in Computational Wave Propagation: Direct and Inverse Problems*, eds. M. Ainsworth, P. Davies, D. Duncan, P. Martin and B. Rynne, Vol. 31, Lecture Notes in Computational Science and Engineering (2003), pp. 1–42.
49. I. Harari and D. Avraham, High-order finite element methods for acoustic problems, *J. Comput. Acoust.* **5**(1) (1997) 33–51.
50. I. Harari and F. Magoules, Numerical investigations of stabilized finite element computations for acoustics, *Wave Motion* **39**(4) (2004) 339–349.
51. I. Harari, M. Slavutin and E. Turkel, Analytical and numerical studies of a finite element PML for the Helmholtz equation, *J. Comput. Acoust.* **8**(1) (2000) 121–137.
52. T. Hughes, J. Cottrell and Y. Bazilevs, Isogeometric analysis: Cad, finite elements, nurbs, exact geometry and mesh refinement, *Comput. Methods Appl. Mech. Eng.* **194**(39–41) (2005) 4135–4195.
53. T. Hughes, A. Reali and G. Sangalli, Duality and unified analysis of discrete approximations in structural dynamics and wave propagation: Comparison of p -method finite elements with k -method {NURBS}, *Comput. Methods Appl. Mech. Eng.* **197**(49–50) (2008) 4104–4124.
54. T. J. Hughes, J. A. Evans and A. Reali, Finite element and {NURBS} approximations of eigenvalue, boundary-value, and initial-value problems, *Comput. Methods Appl. Mech. Eng.* **272** (2014) 290–320.
55. T. Huttunen, P. Gamallo and R. J. Astley, Comparison of two wave element methods for the Helmholtz problem, *Commun. Numer. Methods Eng.* **25**(1) (2009) 35–52.
56. F. Ihlenburg, *Finite Element Analysis of Acoustic Scattering* (Springer, New York, 1998).
57. F. Ihlenburg and I. Babuka, Finite element solution of the Helmholtz equation with high wave number part I: The h -version of the FEM, *Comput. Math. Appl.* **30**(9) (1995) 9–37.
58. F. Ihlenburg and I. Babuska, Finite element solution of the Helmholtz equation with high wave number 2. The h - p version of the FEM, *SIAM J. Numer. Anal.* **34**(1) (1997) 315–358.
59. R. Kechroud, X. Antoine and A. Soulaïmani, Numerical accuracy of a Padé-type non-reflecting boundary condition for the finite element solution of acoustic scattering problems at high-frequency, *Int. J. Numer. Methods Eng.* **64**(10) (2005) 1275–1302.
60. R. Kechroud, A. Soulaïmani and X. Antoine, A performance study of plane wave finite element methods with a padé-type artificial boundary condition in acoustic scattering, *Adv. Eng. Soft.* **40**(8) (2009) 738–750.
61. O. Laghrouche and P. Bettess, Short wave modeling using special finite elements, *J. Comput. Acoust.* **08**(01) (2000) 189–210.
62. P. Langer, M. Maeder, C. Guist, M. Krause and S. Marburg, More than six elements per wavelength: The practical use of structural finite element models and their accuracy in comparison with experimental results, *J. Comput. Acoust.* **25**(4) (2017) 1750025.
63. H. Lian, P. Kerfriden and S. P. A. Bordas, Implementation of regularized isogeometric boundary element methods for gradient-based shape optimization in two-dimensional linear elasticity, *Int. J. Numer. Methods Eng.* **106**(12) (2016) 972–1017.
64. H. Lian, R. Simpson and S. Bordas, Stress analysis without meshing: Isogeometric boundary-element method, *Proc. Inst. Civ. Eng., Eng. Comput. Mech.* **166** (2012) 88–89.
65. Y. Liu, *Fast Multipole Boundary Element Method: Theory and Applications in Engineering* (Cambridge University Press, Cambridge, 2009).
66. S. Marburg, Six boundary elements per wavelength: Is that enough? *J. Comput. Acoust.* **10**(1) (2002) 25–51.
67. S. Marburg, The Burton and Miller method: Unlocking another mystery of its coupling parameter, *J. Comput. Acoust.* **24**(1) (2015) 1550016.

68. S. Marburg, A pollution effect in the boundary element method for acoustic problems, *J. Theor. Comput. Acoust.* **26**(2) (2018) 1850018.
69. S. Marburg and S. Schneider, Influence of element types on numeric error for acoustic boundary elements, *J. Comput. Acoust.* **11**(3) (2003) 363–368.
70. M. Medvinsky and E. Turkel, On surface radiation conditions for an ellipse, *J. Comput. Appl. Math.* **234**(6) (2010) 1647–1655.
71. F. A. Milinazzo, C. A. Zala and G. H. Brooke, Rational square-root approximations for parabolic equation algorithms, *J. Acoust. Soc. Am.* **101**(2) (1997) 760–766.
72. L. Moheit and S. Marburg, Infinite elements and their influence on normal and radiation modes in exterior acoustics, *J. Comput. Acoust.* **25**(4) (2017) 1650020.
73. J.-C. Nédélec, *Acoustic and Electromagnetic Equations: Integral Representations for Harmonic Problems*, Vol. 144, Applied Mathematical Sciences (Springer-Verlag, New York, 2001).
74. V. P. Nguyen, C. Anitescu, S. P. Bordas and T. Rabczuk, Isogeometric analysis: An overview and computer implementation aspects, *Math. Comput. Simul.* **117** (2015) 89–116.
75. A. Oberai and P. Pinsky, A numerical comparison of finite element methods for the Helmholtz equation, *J. Comput. Acoust.* **8**(1) (2000) 211–221.
76. P. Ortiz and E. Sanchez, An improved partition of unity finite element model for diffraction problems, *Int. J. Numer. Methods Eng.* **50**(12) (2001) 2727–2740.
77. V. Puzyrev, Q. Deng and V. Calo, Dispersion-optimized quadrature rules for isogeometric analysis: Modified inner products, their dispersion properties, and optimally blended schemes, *Comput. Methods Appl. Mech. Eng.* **320** (2017) 421–443.
78. Y. Saad, *Iterative Methods for Sparse Linear Systems*, 2nd edn. (Society for Industrial and Applied Mathematics, Philadelphia, 2003).
79. R. Simpson, S. Bordas, H. Lian and J. Trevelyan, An isogeometric boundary element method for elastostatic analysis: 2D implementation aspects, *Comput. Struct.* **118** (2013) 2–12.
80. R. Simpson, S. Bordas, J. Trevelyan and T. Rabczuk, A two-dimensional isogeometric boundary element method for elastostatic analysis, *Comput. Methods Appl. Mech. Eng.* **209** (2012) 87–100.
81. L. L. Thompson, A review of finite-element methods for time-harmonic acoustics, *J. Acoust. Soc. Am.* **20** (2006) 1315–1330.
82. L. L. Thompson and P. M. Pinsky, Complex wavenumber fourier analysis of the p -version finite element method, *Comput. Mech.* **13**(4) (1994) 255–275.
83. L. L. Thompson and P. M. Pinsky, A galerkin least-squares finite element method for the two-dimensional Helmholtz equation, *Int. J. Numer. Methods Eng.* **38**(3) (1995) 371–397.
84. S. Tsynkov, Numerical solution of problems on unbounded domains: A review, *Appl. Numer. Math.* **27**(4) (1998) 465–532.
85. E. Turkel, Boundary conditions and iterative schemes for the Helmholtz equation in unbounded region, in *Computational Methods for Acoustics Problems* (Saxe-Coburg Publications, UK, 2008), pp. 127–158.
86. E. Turkel, C. Farhat and U. Hetmaniuk, Improved accuracy for the Helmholtz equation in unbounded domains, *Int. J. Numer. Methods Eng.* **59**(15) (2004) 1963–1988.
87. W. A. Wall, M. A. Frenzel and C. Cyron, Isogeometric structural shape optimization, *Comput. Methods Appl. Mech. Eng.* **197**(33–40) (2008) 2976–2988.
88. K. Zhao, M. N. Vouvakis and J.-F. Lee, The adaptive cross approximation algorithm for accelerated method of moments computations of EMC problems, *IEEE Trans. Electromagn. Compat.* **47**(4) (2005) 763–773.

Appendix A. Pseudo-Code of the 1D Problem

The stiffness matrix for a single element is calculated and assembled into the global matrix following these steps:

- set $K = 0$;
- loop over number of elements;
- loop over Gaussian points $\tilde{\xi}_i, \tilde{w}_i$
 - (a) find the parametric coordinate $\xi = \tilde{\phi}^e(\tilde{\xi}_j)$;
 - (b) compute the basis function R_a^e ($a = 1, \dots, p + 1$) at point ξ ;
 - (c) define vector $\mathbf{R} = [R_1^e, R_2^e, \dots, R_{p+1}^e]$;
 - (d) compute the basis function derivatives $R_{a,\xi}^e$ ($a = 1, \dots, p + 1$) at point ξ ;
 - (e) define vector $\mathbf{R}_\xi = [R_{1,\xi}^e, R_{2,\xi}^e, \dots, R_{p+1,\xi}^e]$;
 - (f) compute $|J_\xi| = \|\mathbf{R}_\xi \mathbf{P}\|$;
 - (g) compute $|J_{\tilde{\xi}}| = 0.5(\xi_{i+1} - \xi_i)$;
 - (h) compute shape function derivatives $\mathbf{R}_x = J_\xi^{-1} \mathbf{R}_\xi^T$;
 - (i) set $\mathbf{k}^e = \mathbf{k}^e + \mathbf{R}_x \mathbf{R}_x^T |J_\xi| |J_{\tilde{\xi}}| \tilde{w}_j - k^2 \mathbf{R} \mathbf{R}^T |J_\xi| |J_{\tilde{\xi}}| \tilde{w}_j$;
 - (j) end of both loops;

then, the Neumann boundary condition is applied and the resulting linear system is solved to find the estimated solution in B-Spline FEM.